

# Mesh-clustered Gaussian process emulator for partial differential equation systems

Chih-Li Sung<sup>\*,a</sup>, Wenjia Wang<sup>\*,b</sup>, Liang Ding<sup>c</sup>, Xingjian Wang<sup>d</sup>

<sup>a</sup>Michigan State University

<sup>b</sup>Hong Kong University of Science and Technology (Guangzhou)

<sup>c</sup>Fudan University   <sup>d</sup>Tsinghua University

## Abstract

Partial differential equations (PDEs) have become an essential tool for modeling complex physical systems. Such equations are typically solved numerically via mesh-based methods, such as finite element methods, the outputs of which consist of the solutions on a set of mesh nodes over the spatial domain. However, these simulations are often prohibitively costly to survey the input space. In this paper, we propose an efficient emulator that simultaneously predicts the outputs on a set of mesh nodes, with theoretical justification of its uncertainty quantification. The novelty of the proposed method lies in the incorporation of the mesh node coordinates into the statistical model. In particular, the proposed method segments the mesh nodes into multiple clusters via a Dirichlet process prior and fits a Gaussian process model in each. Most importantly, by revealing the underlying clustering structures, the proposed method can extract valuable flow physics present in the systems that can be used to guide further investigations. Real examples are demonstrated to show that our proposed method has smaller prediction errors than its main competitors, with competitive computation time, and identifies interesting clusters of mesh nodes that exhibit coherent input-output relationships and possess physical significance, such as satisfying boundary conditions. An R package for the proposed methodology is provided in an open repository.

*Keywords:* Computer Experiments; Mixture Model; Finite Element Method; Error Analysis; Functional Output; Dirichlet process; Uncertainty Quantification.

---

\*These authors contributed equally to the manuscript. CS gratefully acknowledges funding from NSF DMS 2113407. WW gratefully acknowledges funding from NSFC grant 12101149.

# 1 Introduction

Computer models have become essential to study physical systems that are expensive or infeasible, and have been successfully applied in a variety of scientific research, ranging from cell adhesion (Sung et al., 2020) to rocket injector (Mak et al., 2018). Typically, a physical system is described by a computer model consisting of a series of partial differential equations (PDEs) (Evans, 2010) and simulated in a two- or three-dimensional space. For instance, in Wang et al. (2018), the governing PDEs are used to simulate the characteristics and transition mechanisms of a three-dimensional swirling flow in a cylindrical chamber.

These PDE systems are typically solved by numerical methods, such as finite element methods (FEMs) or a collocation method (Fornberg and Flyer, 2015), based on some predefined mesh specifications in a two- or three-dimensional space, and the simulation outputs are obtained at these mesh node coordinates (also called *grid points* (Mak et al., 2018; Tan, 2018a)). The number of nodes is usually fairly large to ensure the numeric accuracy of PDE solutions. Such computer simulations, however, are often too prohibitively costly for input space exploration. For instance, the high-fidelity simulation in Mak et al. (2018) generates around 100,000 grid points and takes six days of computation time for a given simulation input. Thus, it is essential to develop a cheaper statistical *emulator* as a surrogate model that approximates the simulation outputs in a timely fashion.

The paper focuses on developing an efficient emulator for a series of simulation outputs at *many* coordinates in a PDE system. A popular statistical emulator for computer simulations is through Gaussian process (GP) modeling (Santner et al., 2018; Gramacy, 2020), which provides an accurate approximation to the relationship between simulation output and inputs, with appropriate uncertainty quantification based on its predictive variance; however, the conventional GP is mainly for predicting a scalar output and is not directly applicable to the context of many outputs. One idea is to simultaneously emulate the output at each coordinate separately using independent GPs, which is discussed in Qian et al. (2008), Conti and O’Hagan (2010), and Lee et al. (2011, 2012), and another idea is using GPs with a special shared covariance structure (Gu et al., 2016). These methods, however, cannot naturally provide predictions at *any* coordinates in the domain of interest and do not incorporate the information of mesh node locations into the models. Another idea is to perform dimension reduction to approximate the simulation outputs using basis expansion, such as functional

principal component analysis (Ramsay and Silverman, 2005) or Karhunen-Loève expansion (Karhunen, 1947; Loève, 1955), and then fit GP models on the coefficients, the number of which is usually much less than the number of outputs. The methods adopting this idea include Higdon et al. (2008), Rougier (2008), Rougier et al. (2009), Marrel et al. (2011), Mak et al. (2018), and Tan (2018a). Such methods, however, achieve the dimension reduction by a *finite* truncation of the basis functions, and the approximation error can introduce additional bias to the predictions.

In this paper, we propose a novel, efficient emulator, called *mesh-clustered Gaussian process* (**mcGP**) emulator, for predicting the outputs at many coordinates in a PDE system by incorporating the information of mesh node coordinates. Specifically, instead of fitting separate GPs at each node coordinate, the proposed method makes use of the divide-and-conquer idea, which segments the node coordinates into *clusters* with a soft-assignment clustering approach, in each of which *one* GP is fitted. In particular, the Dirichlet process (DP) prior is adopted that allows for *infinite* clusters for the proposed mixture model without the need of specifying the number of clusters. In addition, a basis expansion representation is employed for mesh-based simulations and the GPs are used to model the coefficients, which allows us to emulate the entire surface of the domain of interest. Note that, this basis expansion *does not* perform dimension reduction, so no additional bias will be introduced to our predictions. Importantly, given such a sophisticated mixture model, the proposed method can be fitted efficiently by adopting the variational Bayesian inference method (Jordan et al., 1999; Wainwright and Jordan, 2008), which provides an analytical approximation to the posterior probability of the latent variables and parameters.

In addition to efficient emulation, our method also provides two important features. First, our method enables efficient uncertainty quantification for emulation with theoretical guarantees. In particular, we provide the error analysis that not only considers the uncertainty from the emulator given limited training samples, but also accounts for the numeric error from the numerical methods for solving PDEs. Second, by revealing the clustering structures, the proposed method provides valuable insights about the underlying physics present in the system. Unlike traditional reduced-basis methods for flow simulations in physics and engineering, such as proper orthogonal decomposition (POD) (Lumley, 1967), which are unsupervised learning methods purely based on the flow data, the latent clustering structure by the proposed method is determined by both simulation inputs and outputs as

in Joseph and Mak (2021) and Sung et al. (2023), which can be used to separate a simulated flow into key instability structures, each with its corresponding spatial features.

It is important to note that recent developments in the field of finite element methods have led to the emergence of the *statistical finite elements* (statFEM) approach, which holds promise in advancing uncertainty quantification and model predictions by a Bayesian statistical construction of finite element methods. See, for example, Duffin et al. (2021), Girolami et al. (2021) and Akyildiz et al. (2022). Specifically, the statFEM approach employs the prior probability density for the finite element method by solving stochastic PDEs, and uses measurement data to infer the posterior finite elements. In contrast, our focus in this paper is primarily on the development of an efficient surrogate model using multiple evaluations of finite element simulations for solving deterministic PDEs, providing a faster alternative to costly finite element simulations.

The rest of this article is organized as follows. Section 2 provides a brief overview of PDE systems and mesh-based simulations. The proposed model is introduced in Section 3, and its error analysis is developed in Section 4. Real examples are demonstrated in Section 5. Section 6 concludes with directions for future work. Theoretical proofs, and the R (R Core Team, 2018) code for reproducing the numerical results, are provided in Supplementary Materials.

## 2 PDE systems and mesh-based simulations

Partial differential equations (PDEs) are an essential tool in the description of complex systems that are based on rigorous and well understood scientific principles. A PDE system typically can be expressed by a set of partial differential equations with boundary conditions, and the solutions are often dependent on certain inputs of interest, which we denote as  $\mathbf{x} \in \chi \subset \mathbb{R}^p$  with  $\chi$  being compact and convex. Specifically, a PDE system can be written in the form of

$$\begin{cases} \mathcal{L}(u(\mathbf{s}); \mathbf{x}) = f(\mathbf{s}; \mathbf{x}), & \mathbf{s} \in \Omega \\ \mathcal{G}(u(\mathbf{s}); \mathbf{x}) = g(\mathbf{s}; \mathbf{x}), & \mathbf{s} \in \partial\Omega, \end{cases} \quad (1)$$

where  $\Omega$  is a compact domain in  $\mathbb{R}^d$  with a Lipschitz boundary denoted by  $\partial\Omega$ ,  $\mathcal{L}(\cdot; \mathbf{x})$  and  $\mathcal{G}(\cdot; \mathbf{x})$  are differential operators on  $\Omega$  and  $\partial\Omega$  given the input  $\mathbf{x}$ , respectively,  $f(\cdot; \mathbf{x})$  and

$g(\cdot; \mathbf{x})$  are two known functions on  $\Omega$  and  $\partial\Omega$  with the input  $\mathbf{x}$ , and  $u(\mathbf{s})$  is the solution to the partial differential equations (1). Given the input  $\mathbf{x}$ , the exact solution to the equations, denoted by  $u_0(\mathbf{s}, \mathbf{x})$ , usually cannot be written explicitly. Instead, numerical methods are used to approximate the exact solutions, for which the mesh-based numerical methods are most widely used, including the finite difference method (FDM), finite volume method (FVM), and finite element method (FEM) (Brenner and Scott, 2007; Tekkaya and Soyarslan, 2019). The extensions to *mesh-free* methods, such as the collocation method (Golberg et al., 1999; Wendland, 1998; Fasshauer, 1999; Wendland, 1999; Fasshauer, 1996), are straightforward and will be discussed in the remarks. Specifically, mesh-based simulations subdivide a large system into smaller, simpler parts by a particular space discretization in the space dimensions, which is implemented by the construction of a *mesh* of the object. Figure 1 demonstrates a mesh specification for a 2-dimensional FEM problem, in which the triangular elements (Figure 1C) connect all characteristic points (called *nodes*) that lie on their circumference, and this connection is a set of equations called *shape functions*.

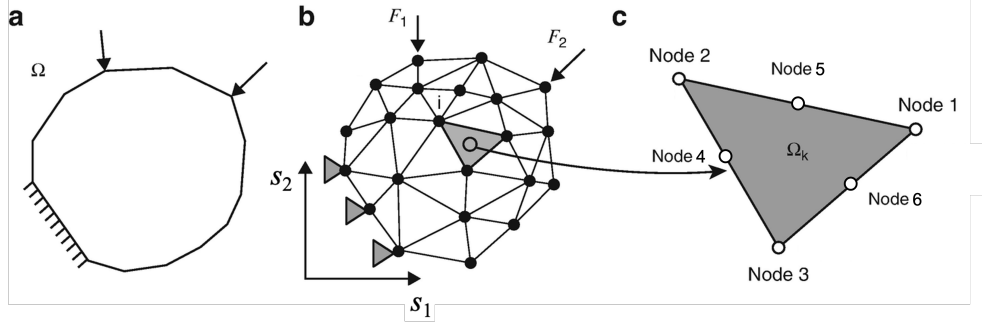


**Figure 1:** Introduction of finite element method (modified from Tekkaya and Soyarslan (2019)).

Suppose that there are  $N$  nodes in this mesh-based simulation, the coordinates of which are denoted by  $\mathbf{S}_N = (\mathbf{s}_1, \mathbf{s}_2, \dots, \mathbf{s}_N)$ , where  $\mathbf{s}_j \in \Omega \cup \partial\Omega$ . The numerical solutions can be expressed as

$$u_N(\mathbf{s}, \mathbf{x}) = \sum_{j=1}^N \beta_j(\mathbf{x}) v_j(\mathbf{s}), \quad (2)$$

where  $v_j(\mathbf{s})$  is the (known) shape function depending on the discretization, and  $\beta_j(\mathbf{x})$  is the corresponding coefficients, which is independent of  $\mathbf{s}$ . The shape function has the Kronecker Delta property, that is,  $v_j(\mathbf{s}_i) = 1$  if  $i = j$  and  $v_j(\mathbf{s}_i) = 0$  if  $i \neq j$ . This ensures that the

function interpolates the solution at the mesh nodes, i.e.,  $u_N(\mathbf{s}_j; \mathbf{x}) = \beta_j(\mathbf{x})$  for  $j = 1, \dots, N$ . In other words, the solution of the PDE at the mesh node  $\mathbf{s}_j$  is equivalent to  $\beta_j(\mathbf{x})$ . As an example, for a triangular element with six nodes as in Figure 1C, the *quadratic* shape functions, which will be adopted in our later implementation in Section 5, can be defined as:

$$\begin{aligned} v_1(\mathbf{s}) &= \xi_1(\mathbf{s})(2\xi_1(\mathbf{s}) - 1), & v_2(\mathbf{s}) &= \xi_2(\mathbf{s})(2\xi_2(\mathbf{s}) - 1), & v_3(\mathbf{s}) &= \xi_3(\mathbf{s})(2\xi_3(\mathbf{s}) - 1), \\ v_4(\mathbf{s}) &= 4\xi_1(\mathbf{s})\xi_2(\mathbf{s}), & v_5(\mathbf{s}) &= 4\xi_2(\mathbf{s})\xi_3(\mathbf{s}), & v_6(\mathbf{s}) &= 4\xi_1(\mathbf{s})\xi_3(\mathbf{s}), \end{aligned} \quad (3)$$

where  $\xi_1, \xi_2$ , and  $\xi_3$  represent the barycentric coordinates associated with the three vertices (Nodes 1, 2, and 3, respectively), which are given by  $\xi_j(\mathbf{s}) = a_j + b_j s_1 + c_j s_2$ , where  $a_j, b_j$ , and  $c_j$  are determined based on the geometry and orientation of the triangle, and ensure that the shape functions satisfy the property that they are equal to 1 at the corresponding nodes and equal to 0 at the other nodes. This formulation can be easily extended to multiple triangular elements; we refer more detailed information and variations of shape functions to Bathe (2006).

The coefficients are obtained by solving a linear system,

$$L(\mathbf{x})\boldsymbol{\beta}_N(\mathbf{x}) = b(\mathbf{x}), \quad (4)$$

where  $\boldsymbol{\beta}_N(\mathbf{x}) = (\beta_1(\mathbf{x}), \dots, \beta_N(\mathbf{x}))^T$  is a vector of the coefficients, and  $L(\mathbf{x}) \in \mathbb{R}^{N \times N}$  is the *stiffness matrix* and  $b(\mathbf{x}) \in \mathbb{R}^N$  is the *load vector*, both of which are determined by the numerical method.

The main challenge of mesh-based simulations is that directly solving the PDE system for any input  $\mathbf{x}$ , or equivalently, solving the linear system (4), can be computationally demanding (e.g., the high-fidelity simulation in Mak et al. (2018)). Thus, an efficient emulator that can approximate the solution,  $u_N(\mathbf{s}, \mathbf{x})$ , for any  $\mathbf{s} \in \Omega, \mathbf{x} \in \chi$ , is called for.

### 3 Mesh-clustered Gaussian process (mcGP) emulator

From (2), since emulating  $u_N(\mathbf{s}; \mathbf{x})$  is equivalent to emulating  $\{\beta_j(\mathbf{x})\}_{j=1}^N$  (because  $v_j$  is a known function), we aim to build an efficient emulator that approximates  $\boldsymbol{\beta}_N(\mathbf{x}) := \{\beta_j(\mathbf{x})\}_{j=1}^N$  for any  $\mathbf{x} \in \chi$ . Suppose that  $n$  computer simulations with the inputs,  $\mathbf{x}_1, \dots, \mathbf{x}_n$ ,

are conducted, and their corresponding solutions at the  $N$  nodes are  $\{\boldsymbol{\beta}_N(\mathbf{x}_i)\}_{i=1}^n$ . Clearly, this is a multi-output regression problem, because for each input  $\mathbf{x}_i$ , the output  $\boldsymbol{\beta}_N(\mathbf{x}_i)$  returns a vector of size  $N$ , where  $N$  can be fairly large. To this end, we propose an efficient emulator that couples over clusters of Gaussian process (GP) emulators, with the aid of the mesh specification to find the clustering structure.

To begin, we briefly introduce the GP emulator in the following subsection.

### 3.1 Gaussian process (GP) emulator

A GP is a popular tool for building an emulator for computer experiments (Santner et al., 2018; Gramacy, 2020) due to its flexibility and the capability of uncertainty quantification through the predictive distribution. Specifically, suppose that we aim to emulate the single output  $\beta_j(\mathbf{x})$ , then the function  $\beta_j$  can be assumed to have a GP prior with zero mean and a positive-definite covariance function,  $K_j(\cdot, \cdot) : \mathbb{R}^p \times \mathbb{R}^p \rightarrow \mathbb{R}$ . The covariance function often has the form of  $K_j(\cdot, \cdot) = \tau_j^2 \Phi_{\boldsymbol{\theta}_j}(\cdot, \cdot)$ , where  $\tau_j^2$  is a positive scale and  $\Phi_{\boldsymbol{\theta}_j}$  is a positive-definite correlation function that depends on some hyperparameters  $\boldsymbol{\theta}_j$ . We denote such a GP as

$$\beta_j(\mathbf{x}) \sim \mathcal{GP}(0, \tau_j^2 \Phi_{\boldsymbol{\theta}_j}(\mathbf{x}, \mathbf{x}')).$$

Denote  $\beta_j(\mathbf{x}_i) = b_{ij}$  and  $\mathbf{b}_j = (b_{1j}, \dots, b_{nj})^T$ , then the observations  $\mathbf{b}_j$  follow an  $n$ -dimensional multivariate normal distribution,  $\mathcal{N}_n(0, \tau_j^2 \Phi_{\boldsymbol{\theta}_j}(\mathbf{X}_n, \mathbf{X}_n))$ , where  $\mathbf{X}_n = (\mathbf{x}_1, \dots, \mathbf{x}_n)$  and  $\Phi_{\boldsymbol{\theta}_j}(\mathbf{X}_n, \mathbf{X}_n)$  is an  $n \times n$  matrix with  $(\Phi_{\boldsymbol{\theta}_j}(\mathbf{X}_n, \mathbf{X}_n))_{i,k} = \Phi_{\boldsymbol{\theta}_j}(\mathbf{x}_i, \mathbf{x}_k)$ . To emulate the  $N$  outputs  $\boldsymbol{\beta}_N(\mathbf{x}) = (\beta_1(\mathbf{x}), \dots, \beta_N(\mathbf{x}))^T$ , we assume that each component  $\beta_j(\mathbf{x})$  follow an independent GP prior, meaning that  $\{\mathbf{b}_j\}_{j=1}^N$  follow  $N$  independent multivariate normal distributions.

For a new input  $\mathbf{x}$ , it can be shown that the posterior predictive distribution is a normal distribution with the mean

$$\mathbb{E}[\beta_j(\mathbf{x})|\mathbf{b}_j] = \Phi_{\boldsymbol{\theta}_j}(\mathbf{x}, \mathbf{X}_n) \Phi_{\boldsymbol{\theta}_j}(\mathbf{X}_n, \mathbf{X}_n)^{-1} \mathbf{b}_j \quad (5)$$

and the variance

$$\mathbb{V}[\beta_j(\mathbf{x})|\mathbf{b}_j] = \tau_j^2 (1 - \Phi_{\boldsymbol{\theta}_j}(\mathbf{x}, \mathbf{X}_n) \Phi_{\boldsymbol{\theta}_j}(\mathbf{X}_n, \mathbf{X}_n)^{-1} \Phi_{\boldsymbol{\theta}_j}(\mathbf{x}, \mathbf{X}_n)^T), \quad (6)$$

where  $\Phi_{\boldsymbol{\theta}_j}(\mathbf{x}, \mathbf{X}_n)$  is a  $1 \times n$  matrix with  $(\Phi_{\boldsymbol{\theta}_j}(\mathbf{x}, \mathbf{X}_n))_{1,i} = \Phi_{\boldsymbol{\theta}_j}(\mathbf{x}, \mathbf{x}_i)$ . The posterior mean can be used to predict  $\beta_j(\mathbf{x})$  and the posterior variance can be used to quantify the prediction uncertainty.

Two families of correlation functions are widely used in practice, which are the power exponential correlation functions and Matérn correlation function (Santner et al., 2018; Stein, 1999). For instance, the Matérn correlation function has the form of

$$\Phi_{\boldsymbol{\theta}}(\mathbf{x}_i, \mathbf{x}_j) = \frac{1}{\Gamma(\nu)2^{\nu-1}} (2\sqrt{\nu}\|\mathbf{x}_i - \mathbf{x}_j\|_{\boldsymbol{\theta}})^{\nu} B_{\nu}(2\sqrt{\nu}\|\mathbf{x}_i - \mathbf{x}_j\|_{\boldsymbol{\theta}}), \quad (7)$$

where  $\|a\|_{\boldsymbol{\theta}}^2 = \sum_{k=1}^p (a_k/\theta_k)^2$  with the  $p$ -dimensional lengthscale hyperparameter  $\boldsymbol{\theta} = (\theta_1, \dots, \theta_p)$ ,  $\nu > 0$  is the smoothness parameter (Cramér and Leadbetter, 1967), and  $B_{\nu}$  is the modified Bessel function of the second kind.

## 3.2 Model specification

While it is possible to model multivariate GPs, instead of independent GPs, using a separable covariance function (Bonilla et al., 2007; Qian et al., 2008) or a nonseparable covariate function (Fricker et al., 2013; Svenson and Santner, 2016), which are often called *co-kriging*, fitting these models can be computationally prohibitive when  $N$  is large. In addition, recent studies (Zhang and Cai, 2015; Kleijnen and Mehdad, 2014; Li et al., 2020) have shown that co-kriging could actually yield worse prediction accuracy than the independent (univariate) GPs described in Section 3.1. On the other hand, Gu et al. (2016) considers independent GPs that share the same lengthscale hyperparameters over the  $N$  outputs, i.e.,  $\boldsymbol{\theta}_1 = \dots = \boldsymbol{\theta}_N$ , but assume different  $\tau_j$ 's over the  $N$  outputs.

From the perspective of statistical learning, independent univariate GPs sharing the same hyperparameters over the  $N$  outputs could be underparametrized, while the one sharing different hyperparameters could be overparametrized. To this end, we propose a flexible model that serves as a compromise between the two models:

$$\begin{aligned} \beta_j(\mathbf{x}) &\sim \mathcal{GP}(0, \tau_j^2 \Phi_{\boldsymbol{\theta}_j}(\mathbf{x}, \mathbf{x}')) \quad \text{for } j = 1, \dots, N, \\ \tau_j^2, \boldsymbol{\theta}_j &\sim G, \\ G &\sim \mathcal{DP}(H, \alpha_0), \end{aligned} \quad (8)$$



where  $\mathcal{DP}$  denotes a Dirichlet process (DP) prior (Ferguson, 1973) with a positive real scalar  $\alpha_0$  and  $H$  being a distribution over  $\tau_j^2$  and  $\boldsymbol{\theta}_j$ . The parameter  $\alpha_0$  is often called *concentration* parameter. The smaller  $\alpha_0$  yields more concentrated distributions. The DP prior is a Bayesian nonparametric model and is a popular tool for developing mixture models, which are often called *infinite* mixture models, because such mixture models have a countably infinite number of mixture components; therefore, these models do not require to pre-specify a fixed number of mixture components, which can be difficult to determine in practice. A DP can be constructively defined by the *stick-breaking* construction (Sethuraman, 1994), by which (8) can be equivalently expressed as

$$\beta_j(\mathbf{x})|z_j = k, \tau_k^2, \boldsymbol{\theta}_k \sim \mathcal{GP}(0, \tau_k^2 \Phi_{\boldsymbol{\theta}_k}(\mathbf{x}, \mathbf{x}')) \quad \text{for } j = 1, \dots, N, \quad (9)$$

$$z_j|\gamma_1, \dots, \gamma_\infty \stackrel{\text{iid}}{\sim} \text{Categorical}(\pi_1, \pi_2, \dots, \pi_\infty) \quad \text{for } j = 1, \dots, N, \quad (10)$$

$$\pi_k = \gamma_k \prod_{l=1}^{k-1} (1 - \gamma_l) \quad \text{for } k = 1, 2, \dots, \infty, \quad (11)$$

$$\gamma_k \stackrel{\text{iid}}{\sim} \text{Beta}(1, \alpha_0) \quad \text{for } k = 1, 2, \dots, \infty, \quad (12)$$

$$\tau_k^2, \boldsymbol{\theta}_k \stackrel{\text{iid}}{\sim} H, \quad \text{for } k = 1, 2, \dots, \infty,$$

where “iid” denotes independently and identitically distributed, and “Categorical” and “Beta” denote a categorical distribution and a Beta distribution, respectively. From (9),  $z_j$  is a latent variable indicating the assignment of  $\beta_j(\mathbf{x})$  to the  $k$ -th GP having the hyperparameters  $\boldsymbol{\theta}_k$  and  $\tau_k^2$ , where the number of GPs is countably infinite. This forms an infinite mixture of GPs for multivariate outputs, with the mixing proportion  $\Pr(z_j = k) = \pi_k$ . The proportion  $\pi_k$  is given by (11), which provides the *stick-breaking* representation of a DP as  $G = \sum_{k=1}^{\infty} \pi_k \delta_{(\tau_k^2, \boldsymbol{\theta}_k)}$ , where  $\delta_{(\tau_k^2, \boldsymbol{\theta}_k)}$  is the indicator function whose value is one at location  $(\tau_k^2, \boldsymbol{\theta}_k)$  and zero elsewhere. The proportions  $\{\pi_k\}_{k=1}^{\infty}$  always sum to one and can be resembling the breaking of a unit-length stick into a countably infinite number of pieces (hence the name). That is, a portion of a unit-length stick is broken off according to  $\gamma_k$  and assigned to  $\pi_k$ , so (11) can be understood by considering that after the first  $k - 1$  values have been assigned their portions, the length of the remaining stick is  $\prod_{l=1}^{k-1} (1 - \gamma_l)$ , and this remaining piece is broken according to  $\gamma_k$  and assigned to  $\pi_k$ . It is important to note that because the  $\pi_k$ ’s decrease exponentially quickly, only a small number of components will be

used to model the data a priori, which allows the number of clusters to be automatically determined. More details about DP applications can be found in Neal (1992), Lo (1984), and Rasmussen (2000).

We further let the latent indicator variable be *mesh-dependent*, implying that the clustering structure is determined by the mesh coordinates. Specifically, assume that the node coordinate  $\mathbf{s}_j$  for the cluster  $k$  follows a  $d$ -dimensional multivariate normal distribution,

$$\mathbf{s}_j|z_j = k \sim \mathcal{N}_d(\boldsymbol{\mu}_k, \boldsymbol{\Sigma}_k^{-1}), \quad (13)$$

where  $\boldsymbol{\mu}_k$  is the mean and  $\boldsymbol{\Sigma}_k$  is the inverse covariance, and their priors are a multivariate normal distribution and a Wishart distribution, respectively, that is,

$$\boldsymbol{\mu}_k \sim \mathcal{N}_d(\boldsymbol{\mu}_0, \boldsymbol{\Sigma}_0^{-1}), \quad \boldsymbol{\Sigma}_k \sim \mathcal{W}(\mathbf{W}_0, \kappa_0), \quad (14)$$

where  $\boldsymbol{\mu}_0, \boldsymbol{\Sigma}_0, \mathbf{W}_0$  and  $\kappa_0$  are fixed hyperparameters. Unlike a conditional model where  $z_j|\mathbf{s}_j$  is employed to model the dependence of  $z_j$  and  $\mathbf{s}_j$ , the model (13) is a *generative* model (Ng and Jordan, 2001) that models the dependence, which learns  $\mathbf{s}_j|z_j$  to subsequently infer the posterior of  $z_j$  by their joint distribution. This generative method offers a consistent way of specifying each component’s responsibility for a given node coordinate, as pointed out in Meeds and Osindero (2005) and Sun and Xu (2010). It is also worth noting that the multivariate normal assumption for  $\mathbf{s}_j|z_j$  aligns with a well-known classification method—quadratic discriminant analysis (QDA), which implies that mesh nodes will be categorized into distinct classes/clusters based on this model choice.

**Remark 3.1.** *Although the latent indicator variable is mesh-dependent particularly for mesh-based simulations, the idea can also be extended to mesh-free numerical methods, such as the collocation method (Wendland, 1998), where the basis function  $v_j(\mathbf{s})$  becomes radial basis functions with some given knot locations and the knots can then be clustered in a similar manner. In addition, the idea can be naturally extended to other applications than solving PDEs that may have different dependence structures, such as the spatially-related dependence structure between proximate sites in Dahl and Bonilla (2019) and the network-related dependence structure in Wilson et al. (2012).*

Combining the above models, a graphical representation of the proposed model is given

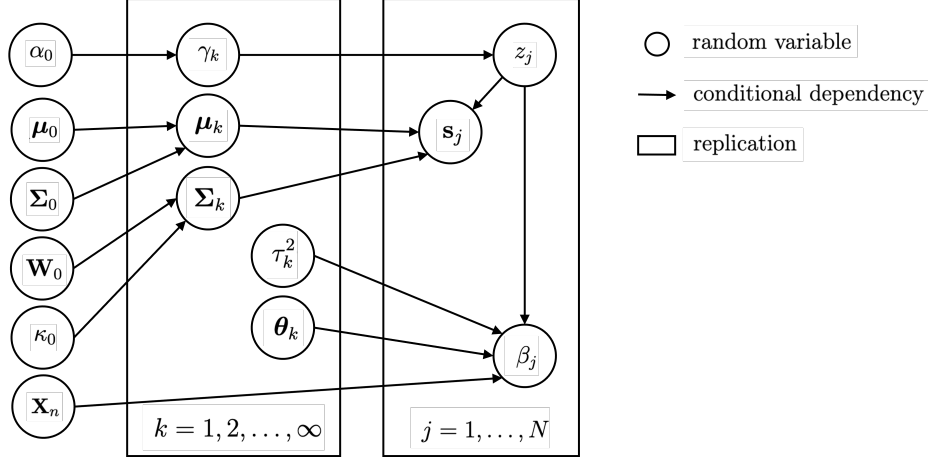


**Figure 2:** Graphical model representation of *mcGP*.

in Figure 2. It should be noted that the proposed *mcGP* is intrinsically different from the infinite mixture of GPs in Rasmussen and Ghahramani (2001), Meeds and Osindero (2005) and Sun and Xu (2010). In particular, the mixture model therein focuses on dividing the input space of  $\mathbf{x}$  to address both the problems of computational complexity and stationary assumption for a univariate GP, whereas our proposed method addresses multi-output regression problems by dividing the mesh node coordinates,  $\{\mathbf{s}_j\}_{j=1}^N$ , into regions, within which separate independent, univariate GPs make predictions.

### 3.3 Parameter estimation: Variational inference

Although Markov chain Monte Carlo (MCMC) methods, such as Gibbs sampling, can be naturally used to draw the posterior distribution of hidden variables for DP mixture models (see, e.g., Rasmussen (2000); Neal (2000); Rasmussen and Ghahramani (2001)), they are often computationally demanding. Therefore, variational inference (VI) (Jordan et al., 1999; Ganguly and Earp, 2021) is adopted here to approximate the posterior, which leads to faster computation and efficient scalability.

Denote the parameters  $\tilde{\gamma} = (\gamma_1, \dots, \gamma_\infty)$ ,  $\tilde{\mu} = (\mu_1, \dots, \mu_\infty)$ ,  $\tilde{\Sigma} = (\Sigma_1, \dots, \Sigma_\infty)$  and the latent variable  $\tilde{\mathbf{z}} = (z_1, \dots, z_N)$ , and denote the hyperparameters  $\tilde{\tau}^2 = (\tau_1^2, \dots, \tau_\infty^2)$  and  $\tilde{\theta} = (\theta_1, \dots, \theta_\infty)$ . Similar to Sun and Xu (2010), the hyperparameters  $\tilde{\tau}^2$  and  $\tilde{\theta}$  will be estimated via variational expectation maximization (EM). We first develop the posterior of the hidden variable set, which are denoted by  $\phi := (\tilde{\gamma}, \tilde{\mu}, \tilde{\Sigma}, \tilde{\mathbf{z}})$ .

Denote  $\mathbf{D}$  as the observational data,  $\mathbf{D} = \{\beta_j(\mathbf{x}_1), \dots, \beta_j(\mathbf{x}_n), \mathbf{s}_j\}_{j=1}^N = \{\mathbf{b}_j, \mathbf{s}_j\}_{j=1}^N$ . By the graphical model representation in Figure 2, the joint distribution is

$$\begin{aligned} p(\mathbf{D}, \phi) &= p(\mathbf{D}|\phi)p(\phi) = \left( \prod_{j=1}^N p(\mathbf{b}_j|z_j)p(\mathbf{s}_j, z_j|\tilde{\boldsymbol{\mu}}, \tilde{\boldsymbol{\Sigma}}, \tilde{\gamma}) \right) \times \left( \prod_{k=1}^{\infty} p(\gamma_k)p(\boldsymbol{\mu}_k)p(\boldsymbol{\Sigma}_k) \right) \\ &= \left( \prod_{j=1}^N p(\mathbf{b}_j|z_j)p(\mathbf{s}_j|z_j, \tilde{\boldsymbol{\mu}}, \tilde{\boldsymbol{\Sigma}})p(z_j|\tilde{\gamma}) \right) \times \left( \prod_{k=1}^{\infty} p(\gamma_k)p(\boldsymbol{\mu})p(\boldsymbol{\Sigma}_k) \right), \end{aligned} \quad (15)$$

where  $p(\mathbf{b}_j|z_j)$  is the probability density function (pdf) of the  $n$ -dimensional multivariate normal distribution from (9), i.e.,  $\mathbf{b}_j|z_j = k \sim \mathcal{N}_n(0, \tau_k^2 \Phi_{\boldsymbol{\theta}_k}(\mathbf{X}_n, \mathbf{X}_n))$ ,  $p(\mathbf{s}_j|z_j, \tilde{\boldsymbol{\mu}}, \tilde{\boldsymbol{\Sigma}})$  is the pdf of the multivariate normal distribution from (13),  $p(\gamma_k)$  is the beta distribution from (12), and  $p(\boldsymbol{\mu}_k)$  and  $p(\boldsymbol{\Sigma}_k)$  are the multivariate normal distribution and the Wishart distribution from (14), respectively.

Clearly, the posterior,  $p(\phi|\mathbf{D}) = p(\mathbf{D}, \phi)/p(\mathbf{D})$ , has a complex probability density which cannot be represented in a closed form. To this end, we apply VI to provide an analytical approximation to  $p(\phi|\mathbf{D})$ . Specifically, VI finds a distribution that is restricted to belong to a family of distributions of simpler forms, denoted by  $q(\phi)$ , such that  $q(\phi) \approx p(\phi|\mathbf{D})$ , which is called *variational distribution*. This can be done by finding the variational distribution that minimizes the Kullback-Leibler (KL) divergence of  $q(\phi)$  from  $p(\phi|\mathbf{D})$ :

$$\begin{aligned} \text{KL}(q(\phi)||p(\phi|\mathbf{D})) &= \mathbb{E}_q[\log(q(\phi))] - \mathbb{E}_q[\log p(\phi|\mathbf{D})] \\ &= \mathbb{E}_q[\log(q(\phi))] - \mathbb{E}_q[\log p(\mathbf{D}, \phi)] + \log p(\mathbf{D}), \end{aligned}$$

which is equivalent to maximizing

$$\text{ELBO}(q) = \mathbb{E}_q[\log p(\mathbf{D}, \phi)] - \mathbb{E}_q[\log(q(\phi))] \quad (16)$$

because  $\log p(\mathbf{D}) = \text{KL}(q(\phi)||p(\phi|\mathbf{D})) + \text{ELBO}(q)$  and  $\log p(\mathbf{D})$  is fixed with respect to  $q(\phi)$ . The function is called *evidence lower bound (ELBO)*, which is a lower bound for the log-evidence of the data (hence the name), that is,  $\log p(\mathbf{D}, \phi) \geq \text{ELBO}(q)$  for any  $q$ . This can be shown by the fact that  $\text{KL}(q(\phi)||p(\phi|\mathbf{D})) \geq 0$  for any  $q$ .

Here we adopt the *mean field approximation* method (see Blei et al. (2017) for more details) to formulate the variational distribution  $q(\phi)$ , which considers the mean-field

variational family where the variables  $\phi$  are mutually independent and each governed by a distinct factor in the variational density. In addition, we approximate the posterior DP by a *truncated* stick-breaking representation as in Ishwaran and James (2001), Blei and Jordan (2006), and Sun and Xu (2010). This can be done by setting  $q(\gamma_K = 1) = 1$  with a fixed value  $K$ , indicating that the stick is no longer broken after  $K - 1$  steps. The length of the remainder of the stick is assigned to  $\pi_K$ , while the lengths of the sticks beyond  $K$  become zero. This implies that the mixing proportion  $\pi_k = 0$  for any  $k > K$ . Together, the mean field approximation method uses the following factorized variational distribution to approximate  $p(\phi|\mathbf{D})$ :

$$q(\phi) = \prod_{k=1}^{\infty} q(\gamma_k) q(\boldsymbol{\mu}_k) q(\boldsymbol{\Sigma}_k) \prod_{j=1}^N q(z_j) = \prod_{k=1}^{K-1} q(\gamma_k) \prod_{k=1}^K q(\boldsymbol{\mu}_k) q(\boldsymbol{\Sigma}_k) \prod_{j=1}^N q(z_j).$$

Given this mean-field variational family, the variational distribution for each  $\omega \in \phi$  can be optimized by maximizing the ELBO using coordinate ascent variational inference (Bishop, 2006), which gives the optimal variational distribution:

$$\log q(\omega) = \mathbb{E}_{\phi \setminus \omega} [\log p(\mathbf{D}, \phi)] + \text{constant}, \quad (17)$$

where the expectation  $\mathbb{E}_{\phi \setminus \omega}$  is with respect to the variational distribution over all variables  $\phi$  except for  $\omega$ . For example, from (15), the optimal variational distribution for  $\gamma_k$  is

$$\begin{aligned} \log q(\gamma_k) &= \mathbb{E}_{\phi \setminus \gamma_k} [\log p(\mathbf{D}, \phi)] + \text{constant} \\ &= \sum_{j=1}^N \mathbb{E}_{\phi \setminus \gamma_k} [\log p(z_j | \tilde{\gamma})] + \log p(\gamma_k) + \text{constant}. \end{aligned}$$

The distribution  $p(z_j|\tilde{\gamma})$  can be found from (10), which follows that

$$\begin{aligned}
\mathbb{E}_{\phi \setminus \gamma_k}[\log p(z_j|\tilde{\gamma})] &= \mathbb{E}_{\phi \setminus \gamma_k}[\log \pi_{z_j}] = \mathbb{E}_{\phi \setminus \gamma_k} \left[ \log \gamma_{z_j} + \sum_{l=1}^{z_j-1} \log(1 - \gamma_l) \right] \\
&= \sum_{k'=1}^{\infty} q(z_j = k') \mathbb{E}_{\phi \setminus \gamma_k}[\log \gamma_{k'}] + \sum_{k'=1}^{\infty} q(z_j = k') \sum_{l=1}^{k'-1} \mathbb{E}_{\phi \setminus \gamma_k}[\log(1 - \gamma_l)] \\
&= \sum_{k'=1}^{\infty} q(z_j = k') \mathbb{E}_{\phi \setminus \gamma_k}[\log \gamma_{k'}] + \sum_{l=1}^{\infty} \sum_{k'=l+1}^{\infty} q(z_j = k') \mathbb{E}_{\phi \setminus \gamma_k}[\log(1 - \gamma_l)] \\
&= q(z_j = k) \log \gamma_k + q(z_j > k) \log(1 - \gamma_k) + \text{constant},
\end{aligned}$$

where the third equation is based on the variational distribution of  $z_j$ , i.e.,  $q(z_j)$ , the fourth equation changes the order of summation, and the last equation holds because the terms  $\mathbb{E}_{\phi \setminus \gamma_k}[\log \gamma_{k'}]$  and  $\mathbb{E}_{\phi \setminus \gamma_k}[\log(1 - \gamma_{k'})]$  are constant with respect to  $\gamma_k$  when  $k' \neq k$ . Since  $p(\gamma_k)$  follows a Beta distribution as in (12), we have

$$\begin{aligned}
\log q(\gamma_k) &= \sum_{j=1}^N q(z_j = k) \log \gamma_k + q(z_j > k) \log(1 - \gamma_k) + (\alpha_0 - 1) \log(1 - \gamma_k) + \text{constant} \\
&= \left( \sum_{j=1}^N q(z_j = k) \right) \log \gamma_k + \left( \sum_{j=1}^N q(z_j > k) + \alpha_0 - 1 \right) \log(1 - \gamma_k) + \text{constant},
\end{aligned}$$

which implies that  $q(\gamma_k)$  follows  $\text{Beta}(\sum_{j=1}^N q(z_j = k) + 1, \sum_{j=1}^N q(z_j > k) + \alpha_0)$ .

The optimal variational distributions for the remaining variables  $\omega \in \phi$  can be derived in a similar manner. The specific results are provided in the E-step of Algorithm 1, and for detailed derivations, we refer to Supplementary Materials S1. Note that the truncation level  $K$  is a variational parameter which can be freely set. Although it is possible to optimize  $K$  with respect to the KL divergence, we hold it fixed as in Blei and Jordan (2006) and Sun and Xu (2010) throughout this paper.

Given the optimal variational distributions, the hyperparameters of the GPs,  $\theta_k$  and  $\tau_k^2$ , can be estimated by maximizing the expected log-likelihood with respect to the approximated distributions, which is called *variational EM* in the literature (Blei et al., 2017). Specifically, since  $\mathbf{b}_j|z_j = k \sim \mathcal{N}_n(0, \tau_k^2 \Phi_{\theta_k}(\mathbf{X}_n, \mathbf{X}_n))$ , the estimates, denoted by  $\hat{\theta}_k$  and  $\hat{\tau}_k^2$ , can be solved

by maximizing

$$\begin{aligned} \mathbb{E}_q[\log p(\mathbf{D}, \boldsymbol{\phi})] = \text{constant} \\ - \frac{1}{2} \left( \sum_{j=1}^N \sum_{k=1}^K q(z_j = k) \left[ n \log \tau_k^2 + \log |\Phi_{\boldsymbol{\theta}_k}(\mathbf{X}_n, \mathbf{X}_n)| + \frac{1}{\tau_k^2} \mathbf{b}_j^T \Phi_{\boldsymbol{\theta}_k}(\mathbf{X}_n, \mathbf{X}_n)^{-1} \mathbf{b}_j \right] \right) \end{aligned} \quad (18)$$

with respect to  $\boldsymbol{\theta}_k$  and  $\tau_k^2$ . The estimators are given in the M-step of Algorithm 1, and the detailed derivations are provided in Supplementary Materials S1. The E- and M-step repeats iteratively by updating the parameters of the variational distributions until the ELBO converges, where the explicit form of ELBO (derived from (16)) is provided in Supplementary Materials S1. In total, each iteration going through all the observations would take at most  $O(KNn^3)$ , which is linear with respect to the number of mesh nodes,  $N$ . This variational EM algorithm as in Algorithm 1 can be implemented via the open source R package `mcGP`.

### 3.4 Prediction

For unknown  $\mathbf{x} \in \chi$ , the predictive posterior distribution of  $\beta_j(\mathbf{x})$  can be constructed as follows,

$$\begin{aligned} p(\beta_j(\mathbf{x}) | \mathbf{D}, \boldsymbol{\phi}, \{\hat{\boldsymbol{\theta}}_k, \hat{\tau}_k^2\}_{k=1}^K) &= \sum_{k=1}^K p(z_j = k | \mathbf{D}, \boldsymbol{\phi}) p(\beta_j(\mathbf{x}) | z_j = k, \mathbf{D}, \hat{\boldsymbol{\theta}}_k, \hat{\tau}_k^2) \\ &\approx \sum_{k=1}^K q(z_j = k) p(\beta_j(\mathbf{x}) | z_j = k, \mathbf{D}, \hat{\boldsymbol{\theta}}_k, \hat{\tau}_k^2), \end{aligned}$$

where the approximation replaces  $p(z_j = k | \mathbf{D}, \boldsymbol{\phi})$  with its variational distribution  $q(z_j = k)$  as in Sun and Xu (2010), and  $p(\beta_j(\mathbf{x}) | z_j = k, \mathbf{D}, \{\hat{\boldsymbol{\theta}}_k, \hat{\tau}_k^2\}_{k=1}^K)$  is the pdf of a normal distribution with the posterior mean (5) and the posterior variance (6) by replacing  $\boldsymbol{\theta}_j$  and  $\tau_j^2$  with  $\hat{\boldsymbol{\theta}}_k$  and  $\hat{\tau}_k^2$ , respectively. Thus, since  $u_N(\mathbf{s}, \mathbf{x}) = \sum_{j=1}^N \beta_j(\mathbf{x}) v_j(\mathbf{s})$ , the posterior mean of  $u_N(\mathbf{s}, \mathbf{x})$  for any  $\mathbf{s} \in \Omega$  and  $\mathbf{x} \in \chi$ , can be approximated by

$$\hat{u}_N(\mathbf{s}, \mathbf{x}) := \sum_{j=1}^N \sum_{k=1}^K q(z_j = k) v_j(\mathbf{s}) \Gamma_{\hat{\boldsymbol{\theta}}_k}(\mathbf{x}, \mathbf{X}_n) \mathbf{b}_j, \quad (19)$$

where  $\Gamma_{\hat{\boldsymbol{\theta}}_k}(\mathbf{x}, \mathbf{X}_n) = \Phi_{\hat{\boldsymbol{\theta}}_k}(\mathbf{x}, \mathbf{X}_n)\Phi_{\hat{\boldsymbol{\theta}}_k}(\mathbf{X}_n, \mathbf{X}_n)^{-1}$ , and the posterior variance is

$$\sum_{j=1}^N v_j(\mathbf{s})^2 \left( \sum_{k=1}^K q(z_j = k) \left[ \hat{\tau}_k^2 (1 - \Gamma_{\hat{\boldsymbol{\theta}}_k}(\mathbf{x}, \mathbf{X}_n)\Phi_{\hat{\boldsymbol{\theta}}_k}(\mathbf{x}, \mathbf{X}_n)^T) + (\Gamma_{\hat{\boldsymbol{\theta}}_k}(\mathbf{x}, \mathbf{X}_n)\mathbf{b}_j)^2 \right] - \left( \sum_{k=1}^K q(z_j = k) \Gamma_{\hat{\boldsymbol{\theta}}_k}(\mathbf{x}, \mathbf{X}_n)\mathbf{b}_j \right)^2 \right). \quad (20)$$

---

**Algorithm 1** Variational expectation maximization for parameter estimation

---

- 1: • Set the truncation level  $K > 1$  and the hyperparameters  $\alpha_0, \boldsymbol{\mu}_0, \boldsymbol{\Sigma}_0, \mathbf{W}_0$ , and  $\kappa_0$ .
- 2: **repeat**
- 3:    E-step: variational distributions  $q(\gamma_k), q(\boldsymbol{\mu}_k), q(\boldsymbol{\Sigma}_k)$  and  $q(z_j)$ .
- 4:    •  $\gamma_k \sim \text{Beta}(a_k, b_k)$  for  $k = 1, \dots, K-1$ , where

$$a_k = \sum_{j=1}^N q(z_j = k) + 1, \quad b_k = \sum_{j=1}^N q(z_j > k) + \alpha_0.$$

- 5:    •  $\boldsymbol{\mu}_k \sim \mathcal{N}_d((\boldsymbol{\Sigma}_0 + \mathbf{R}_{k2})^{-1}(\boldsymbol{\Sigma}_0\boldsymbol{\mu}_0 + \mathbf{R}_{k1}), (\boldsymbol{\Sigma}_0 + \mathbf{R}_{k2})^{-1})$  for  $k = 1, \dots, K$ , where

$$\mathbf{R}_{k1} = \sum_{j=1}^N q(z_j = k) \mathbb{E}_q[\boldsymbol{\Sigma}_k] \mathbf{s}_j, \quad \mathbf{R}_{k2} = \sum_{j=1}^N q(z_j = k) \mathbb{E}_q[\boldsymbol{\Sigma}_k].$$

- 6:    •  $\boldsymbol{\Sigma}_k \sim \mathcal{W}(\mathbf{W}_k, \kappa_k)$ , where  $\kappa_k = \kappa_0 + \sum_{j=1}^N q(z_j = k)$  and

$$\mathbf{W}_k^{-1} = \mathbf{W}_0^{-1} + \sum_{j=1}^N q(z_j = k) \mathbb{E}_q[(\mathbf{s}_j - \boldsymbol{\mu}_k)(\mathbf{s}_j - \boldsymbol{\mu}_k)^T].$$

- 7:    •  $q(z_j = k) = r_{jk} / \sum_{k=1}^K r_{jk}$  for  $j = 1, \dots, N$  and  $k = 1, \dots, K$  with

$$\begin{aligned} \log r_{jk} &= \mathbb{E}_q[\log \gamma_k] + \sum_{i=1}^{k-1} \mathbb{E}_q[\log(1 - \gamma_i)] + \frac{1}{2}(s_{jk} + t_{jk}), \quad \text{where} \\ s_{jk} &= -d \log(2\pi) + \mathbb{E}_q[\log |\boldsymbol{\Sigma}_k|] - \mathbb{E}_q[(\mathbf{s}_j - \boldsymbol{\mu}_k)^T \boldsymbol{\Sigma}_k (\mathbf{s}_j - \boldsymbol{\mu}_k)] \quad \text{and} \\ t_{jk} &= -n \log(2\pi) - \log \tau_k^2 - \log |\Phi_{\boldsymbol{\theta}_k}(\mathbf{X}_n, \mathbf{X}_n)| - \frac{1}{\tau_k^2} \mathbf{b}_j^T \Phi_{\boldsymbol{\theta}_k}(\mathbf{X}_n, \mathbf{X}_n)^{-1} \mathbf{b}_j. \end{aligned}$$

M-step: estimating the hyperparameters  $\boldsymbol{\theta}_k$  and  $\tau_k^2$ .

- 8:    •  $\boldsymbol{\theta}_k \leftarrow \text{argmin}_{\boldsymbol{\theta}_k} \log |\Phi_{\boldsymbol{\theta}_k}(\mathbf{X}_n, \mathbf{X}_n)| + n \log \sum_{j=1}^N q(z_j = k) \mathbf{b}_j^T \Phi_{\boldsymbol{\theta}_k}(\mathbf{X}_n, \mathbf{X}_n)^{-1} \mathbf{b}_j$
  - 9:    •  $\tau_k^2 \leftarrow \left( \sum_{j=1}^N q(z_j = k) \mathbf{b}_j^T \Phi_{\boldsymbol{\theta}_k}(\mathbf{X}_n, \mathbf{X}_n)^{-1} \mathbf{b}_j \right) / \left( n \sum_{j=1}^N q(z_j = k) \right)$
  - 10: **until** ELBO converges
  - 11: • **return**  $q(z_j = k), \boldsymbol{\theta}_k$  and  $\tau_k^2$  for each  $k$  and  $j$ .
-



The derivation of (20) is provided in Supplementary Materials S2. The posterior mean  $\hat{u}_N(\mathbf{s}, \mathbf{x})$  of (19) is used to predict  $u_N(\mathbf{s}, \mathbf{x})$ , and its error analysis is studied in the next section.

## 4 Error analysis of mcGP emulator

The error analysis is crucial for understanding the uncertainty of the emulator. By the triangle inequality, the norm of the difference between the posterior mean  $\hat{u}_N(\mathbf{s}, \mathbf{x})$  and true solution can be decomposed into *simulation* and *emulation* components:

$$\|u_0 - \hat{u}_N\|_{L_2(\Omega, \chi)} \leq \underbrace{\|u_0 - u_N\|_{L_2(\Omega, \chi)}}_{\text{simulation error}} + \underbrace{\|u_N - \hat{u}_N\|_{L_2(\Omega, \chi)}}_{\text{emulation error}},$$

where the  $L_2$ -norm is defined as  $\|f\|_{L_2(\Omega, \chi)} = (\int_{\Omega} \int_{\chi} f(\mathbf{s}, \mathbf{x})^2 d\mathbf{s} d\mathbf{x})^{1/2}$ . The simulation error measures the discrepancy between the simulated solution  $u_N(\mathbf{s}, \mathbf{x})$  and the ground truth  $u_0(\mathbf{s}, \mathbf{x})$ , and the emulation error is the error for the emulator  $\hat{u}_N(\mathbf{s}, \mathbf{x})$  given limited evaluations of the simulator  $u_N(\mathbf{s}, \mathbf{x})$ . To save the space, we investigate the simulation error and emulation error in Supplementary Materials S3 and S4, respectively, and then apply the error bound to a common PDE problem, *elliptic equations*, in Supplementary Materials S5.

## 5 Numerical studies

Numerical studies are conducted in this section to examine the performance of the proposed method. Specifically, three real-world computer models comprised of partial differential equations are considered, which are solved via FEM using the quadratic shape functions as in (3).

In these numerical studies, the hyperparameters in the priors (12) and (14) can be quite generic without the need of estimation. Similar to Yuan and Neubauer (2009) and Sun and Xu (2010), the hyperparameter  $\boldsymbol{\mu}_0$  in (14) is set to the sample average of the node coordinates  $\mathbf{S}_N$ , and  $\boldsymbol{\Sigma}_0$  are set to the sample inverse covariance of  $\mathbf{S}_N$ ; the parameter  $\kappa_0$  is the number of degrees of freedom under a Wishart distribution, which is set to the dimension of  $\mathbf{s}_j$ , that is,  $\kappa_0 = d$ ; the scale parameter  $\mathbf{W}_0$  of the Wishart distribution is set to

$\Sigma_0/d$  such that the mean of  $\Sigma_k$  is the sample inverse covariance of  $\mathbf{S}_N$ . The concentration parameter  $\alpha_0$  in (12) is set to 0.5.

For each individual GP, Matérn correlation functions (7) is considered. The smoothness parameter  $\nu$  is set to 5/2, which leads to a simplified form of (7):

$$\Phi_{\boldsymbol{\theta}}(\mathbf{x}_i, \mathbf{x}_j) = \left(1 + \sqrt{5}\|\mathbf{x}_i - \mathbf{x}_j\|_{\boldsymbol{\theta}} + \frac{5}{3}\|\mathbf{x}_i - \mathbf{x}_j\|_{\boldsymbol{\theta}}^2\right) \exp\left(-\sqrt{5}\|\mathbf{x}_i - \mathbf{x}_j\|_{\boldsymbol{\theta}}\right).$$

A small nugget parameter is added for numerical stability, which is set to  $g \approx 1.5 \times 10^{-8}$ . The truncation level  $K$  is set to 10. These numerical experiments were performed on a MacBook Pro laptop with Apple M1 Max of Chip and 32 GB of RAM.

Two performance measures are considered to examine the prediction performance. The first measure is the root mean squared error (RMSE) which is calculated as

$$\text{RMSE} = \left( \frac{\sum_{j=1}^N \sum_{i=1}^{n_{\text{test}}} (u_N(\mathbf{s}_j, \mathbf{x}_i^{\text{test}}) - \hat{u}_N(\mathbf{s}_j, \mathbf{x}_i^{\text{test}}))^2}{N n_{\text{test}}} \right)^{1/2}, \quad (21)$$

where  $n_{\text{test}}$  is the number of test input points,  $u_N(\mathbf{s}_j, \mathbf{x}_i^{\text{test}})$  is the numeric solution of the  $i$ -th test input point,  $\mathbf{x}_i^{\text{test}}$ , at the  $j$ -th node location,  $\mathbf{s}_j$ , and  $\hat{u}_N(\mathbf{s}_j, \mathbf{x}_i^{\text{test}})$  is the posterior mean as in (19). The second measure is the average continuous ranked probability score (CRPS) (Gneiting and Raftery, 2007), which is a performance measure for predictive distribution of a scalar observation. Since the predictive distribution is a mixture normal distribution as in Section 3.4, the CRPS can be computed by an analytical formula as in Gruit et al. (2006). For both RMSE and CRPS, lower values indicate better prediction accuracy.

To provide a comprehensive evaluation, we include the following methods for comparison: **uGP**, the independent univariate GPs sharing the same lengthscale hyperparameter ( $\boldsymbol{\theta}_j$ ) but different scale hyperparameters ( $\tau_j^2$ ) across the  $N$  mesh nodes, which is similar to Gu et al. (2016); **iGP**, the independent GPs sharing different hyperparameters ( $\boldsymbol{\theta}_j$  and  $\tau_j^2$ ) across the  $N$  mesh nodes; **pcaGP**, which uses a functional principal component analysis (FPCA) with *truncated* components (Wang et al., 2016):

$$u_N(\mathbf{s}_j, \mathbf{x}_i) \approx u_0(\mathbf{s}_j) + \sum_{l=1}^M \alpha_l(\mathbf{x}_i) \psi_l(\mathbf{s}_j),$$

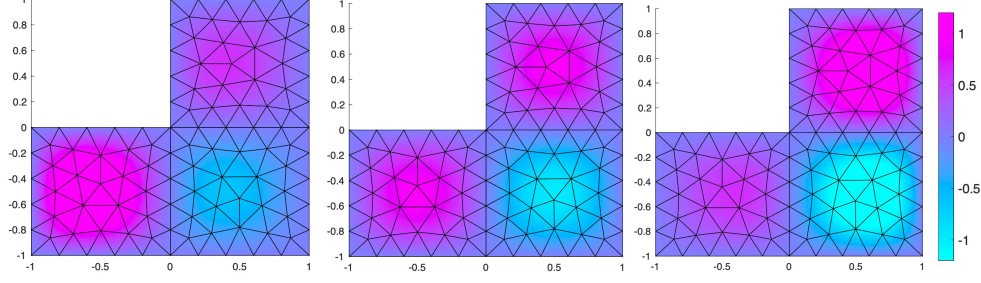


**Figure 3:** Illustration of geometry, mesh, and solutions via FEM for Poisson's equation with (left)  $x = -1$ , (middle)  $x = 0$ , and (right)  $x = 1$ .

with the leading  $M$  eigenfunctions  $\{\psi_l(\mathbf{s})\}_{l=1}^M$ , and the corresponding coefficients  $\{\alpha_l(\mathbf{x}_i)\}$ :

$$\psi_l(\mathbf{s}) = \underset{\substack{\|\phi\|_2=1, \\ \langle \phi, \psi_l \rangle = 0, \forall l < j}}{\operatorname{argmax}} \sum_{i=1}^n \left\{ \int u_N(\mathbf{s}, \mathbf{x}_i) \phi(\mathbf{s}) d\mathbf{s} \right\}^2,$$

$$\alpha_l(\mathbf{x}_i) = \int u_N(\mathbf{s}, \mathbf{x}_i) (\psi_l(\mathbf{s}) - u_0(\mathbf{s})) d\mathbf{s},$$

where  $u_0(\mathbf{s})$  is the mean function, which can be estimated by  $\sum_{i=1}^n u_N(\mathbf{s}, \mathbf{x}_i)/n$ . The number of components,  $M$ , is selected by finding the leading  $M$  eigenfunctions that explain 99% of variance over all  $n$  training cases. Then, iGP is applied to the  $M$  coefficients  $\{\alpha_l(\cdot)\}_{l=1}^M$ . This approach is similar to Dancik and Dorman (2008) and Mak et al. (2018).

## 5.1 Poisson's Equation

In this subsection, we explore the performance of mcGP for emulating a PDE system on an L-shaped membrane based on Poisson's equation, which has broad applicability in electrostatics and fluid mechanics (Evans, 2010). The model is represented as:

$$\Delta u = (x^2 - 2\pi^2)e^{xs_1} \sin(\pi s_1) \sin(\pi s_2) + 2x\pi e^{xs_1} \cos(\pi s_1) \sin(\pi s_2), \quad \mathbf{s} = (s_1, s_2) \in \Omega,$$

where  $x$  is the one-dimensional input variable with  $x \in [-1, 1]$ , the operator  $\Delta$  is defined by  $\Delta = \frac{\partial^2}{\partial s_1^2} + \frac{\partial^2}{\partial s_2^2}$ ,  $\Omega$  is an L-shaped membrane, and the Dirichlet boundary condition,  $u = 0$  on  $\partial\Omega$ , is considered. The geometry and mesh, along with the solutions through FEM when  $x = -1, 0, 1$ , are demonstrated in Figure 3. Partial Differential Equation Toolbox of MATLAB (2021) is used to create the geometry and mesh to solve the equation.

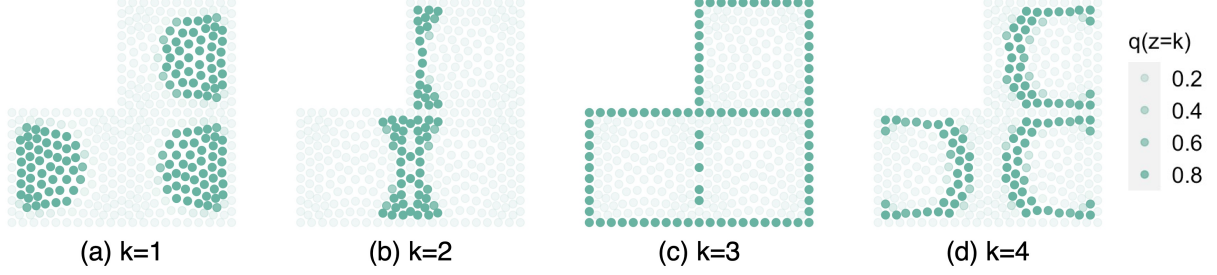


**Figure 4:** Variational distribution  $q(z_j = k)$  in the Poisson's equation experiment.

We conduct a computer experiment of size  $n = 5$ , where the input locations are equally spaced in the input space  $[-1, 1]$ , i.e.,  $x_i = 0.4i - 1.2$  for  $i = 1, \dots, 5$ . The mesh size is set to 0.2, yielding  $N = 401$  mesh nodes as shown in Figure 3. The proposed method is applied to this experimental data. Figure 4 illustrates the variational distribution,  $q(z_j = k)$ , for  $k = 1, \dots, 4$ , and Figure 5 presents the corresponding hyperparameter estimates,  $\hat{\tau}_k^2$  and  $\hat{\theta}_k$ . Note that here  $k = 5, 6, \dots, 10$  are not shown in Figures 4 and 5 because  $q(z_j = k) < 0.001$  for all  $j$ , indicating that only four mixture components are only needed in this mixture model. This shows that, even though the proposed model considers an infinite mixture of GPs throughout a DP prior, the mixing proportions decrease exponentially so quickly that only a small number of components are used to model the data a priori. The fitting result reveals interesting scientific insights. First, the cluster  $k = 3$  has higher probability mass on the nodes at the boundaries and locations of  $s_1 = 0$  and  $s_2 = 0$  (Figure 4), and the corresponding hyperparameters of the GP are  $\hat{\tau}_3^2 \approx 0$  and  $\hat{\theta}_3 \approx 7.5$  (Figure 5), which makes sense because these nodes are related to the solution of 0 based on the boundary condition. Second, the cluster  $k = 1$  features higher probability mass on the nodes in the regions where the magnitude of solutions is the highest and their shapes are similar. The cluster shares high estimates  $\hat{\tau}_1^2$  and  $\hat{\theta}_1$ , indicating the input-output relationship is smooth but the output values in these regions have relatively high variability across different input settings. More interestingly, the cluster  $k = 2$  covers a group of the nodes around  $s_1 = 0$  in the neighbourhood of the cluster  $k = 3$ , while the cluster  $k = 4$  contains a group of nodes in the vicinity of the cluster  $k = 1$ . The example shows that, unlike the traditional reduced-basis methods like proper orthogonal decomposition (POD) (Lumley, 1967), the clustering structures by the proposed method not only provide a useful insight for discovering the underlying physics, but also reveal their shared input-output relationship.

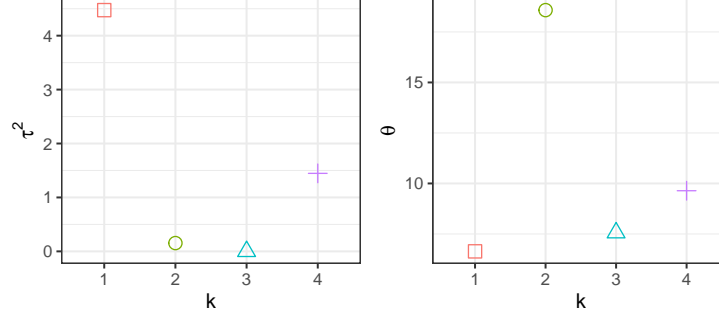


**Figure 5:** Hyperparameter estimates in the Poisson's equation experiment: (left)  $\hat{\tau}_k$ ; (right)  $\hat{\theta}_k$ .

To illustrate the prediction performance, Figure 6 shows the FEM solution (left) at the test input point,  $x^{\text{test}} = -0.25$ , the mcGP posterior mean (middle), and the mcGP posterior standard deviation (right). From visual comparison, the mcGP posterior mean accurately captures the spatial structure of the FEM solution. The prediction uncertainty can be quantified by the posterior standard deviation, where the most uncertain predictions are located in the nodes of cluster  $k = 1$ , which is expected provided that the variation of the outputs are most dynamic with large magnitude in this cluster.

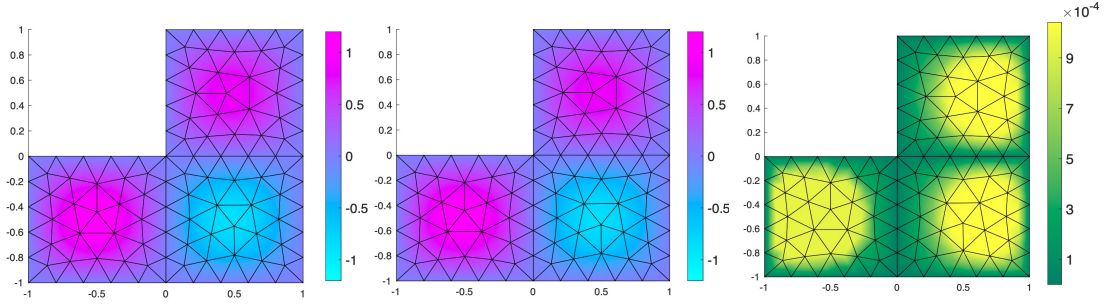


**Figure 6:** Validation performance of mcGP prediction: (left) the real FEM solution when  $x = -0.25$ ; (middle) the mcGP posterior mean; (right) the mcGP posterior standard deviation.

We further examine the prediction and computation performance on 201 test input points equally spaced in  $[-1, 1]$  with various mesh size settings, which are 0.4, 0.2, 0.1, 0.05, and 0.025. The results are presented in Figure 7. From the left two panels, it appears that uGP and pcaGP perform worse than the other two in terms of prediction accuracy (both RMSE and CRPS). While there is no significant difference between iGP and mcGP in the predictive scores, it can be seen that mcGP generally yields lower RMSEs than other methods. The right two panels present the computational cost. It is of no surprise that the proposed

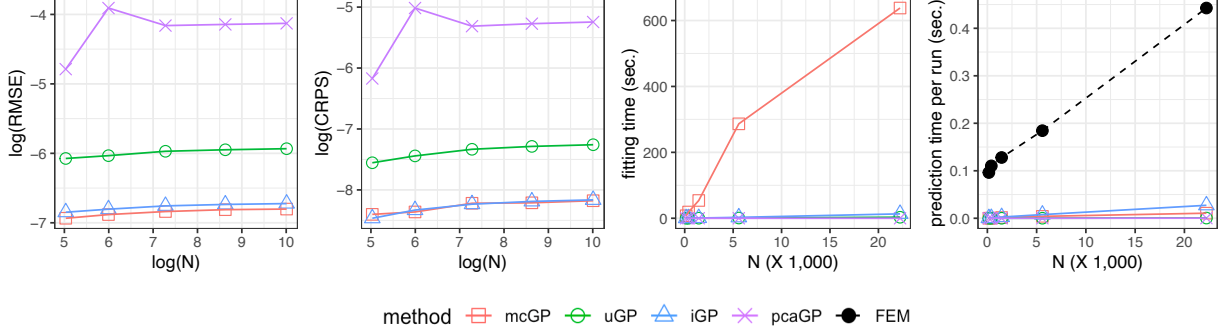


**Figure 7:** Performance comparison in terms of prediction accuracy and computational cost in the Poisson's equation experiment. The left two panels are the prediction performance in terms of RMSE and CRPS in logarithm, and the right two panels are the computational cost in model fitting and predictions.

method requires more fitting time due to the complications of a mixture model; however, as indicated in Section 3.3, the third panel (from the left) shows that the computational cost for fitting mcGP is linear with respect to  $N$ , which is reasonably tractable in practice. Besides, in the context of emulation, the computation for predictions is more of interest, for which it can be seen that the proposed method (and its competitors) can predict much faster than conducting a real FEM simulation.

## 5.2 Laminar flow past a cylinder

In this subsection, we investigate a system of a two-dimensional flow past a circular cylinder, which is a classical and interesting problem in fluid mechanics (Rajani et al., 2009; Seo and Song, 2012). The problem is described by the incompressible Navier-Stokes equations. Two input variables are considered in this study, which are the kinematic viscosity of the fluid ( $x_1$ ) and the freestream velocity in the  $s_1$  direction ( $x_2$ ), where the input space is  $\mathbf{x} = (x_1, x_2) \in [0.01, 1] \times [0.5, 2]$ , which results in laminar flows with Reynolds number between 0.5 and 200. The objective is to predict the velocity component in the  $s_2$  direction ( $v$ ) using the mcGP method. The sample size is prescribed as  $n = 30$ . The sample points are distributed uniformly in the input space following the maximum projection (MaxPro) design method (Joseph et al., 2015), as shown in the left panel of Figure 8. The computer simulations at these points are performed using the FEM solver in the QuickerSim CFD Toolbox (Ltd., 2022). Figure 9 shows the computational mesh and computer solutions of  $v$

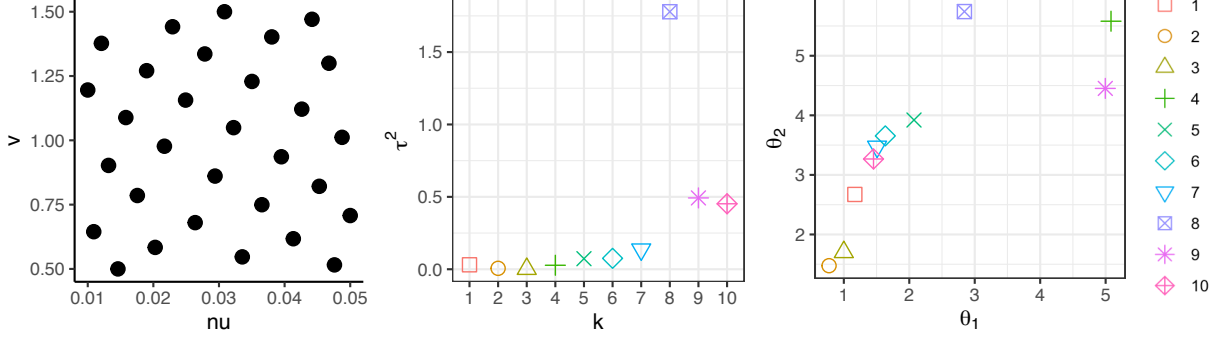


**Figure 8:** The left panel presents the design points in the laminar flow application, and the middle and right panels show the hyperparameter estimates of  $\text{mcGP}$ :  $\hat{\tau}_k$  (middle) and  $\hat{\theta}_k$  (right).

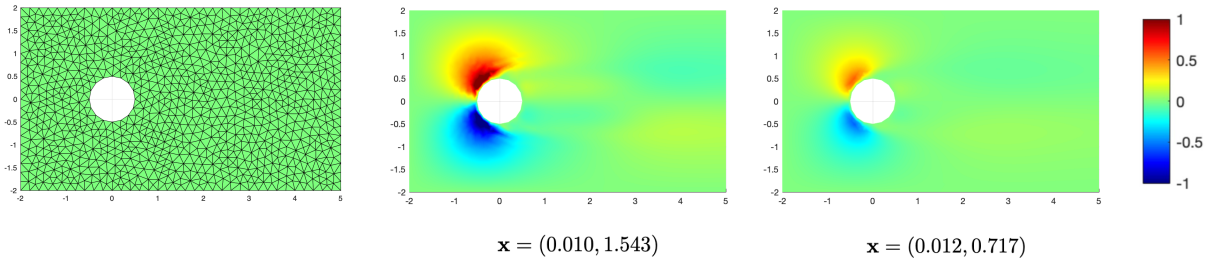


**Figure 9:** The left panel demonstrates the geometry and mesh in the laminar flow application, and the middle and right panels are the two (out of 30) training examples of the simulations, where the input settings are indicated by the values of  $\mathbf{x}$ .

at two different input settings. The total number of mesh nodes is  $N = 3778$ .

The proposed  $\text{mcGP}$  method is applied to this experimental data. Figure 10 illustrates the variational distribution,  $q(z_j = k)$ , for  $j = 1, \dots, N$ , and  $k = 1, \dots, 5, 8, 9, 10$ , and the corresponding hyperparameter estimates are presented in the middle and right panels of Figure 8 for each  $k$ . Note that the clusters  $k = 6$  and  $k = 7$  are not shown here because  $q(z_j = k) < 0.1$  for all  $j$  at these clusters. The result shows that different clusters exhibit high probability mass on the nodes in different fluid regions. For example, the cluster  $k = 4$  has higher probability mass on the nodes at the upstream and vertical boundaries with small  $\hat{\tau}_4^2$  and large  $\hat{\theta}_4$ , while the cluster  $k = 3$  imposes higher probability mass in the downstream boundary and associated neighbouring regions. These two clusters share a common feature of low variation in the vertical velocity, as manifested by Figure 9. The components  $k = 8$  and  $k = 9$  puts higher probability mass in the frontal area of the cylinder with the highest output magnitude, and this comes with the large hyperparameter estimates  $\hat{\tau}_8^2$  and  $\hat{\tau}_9^2$ . In



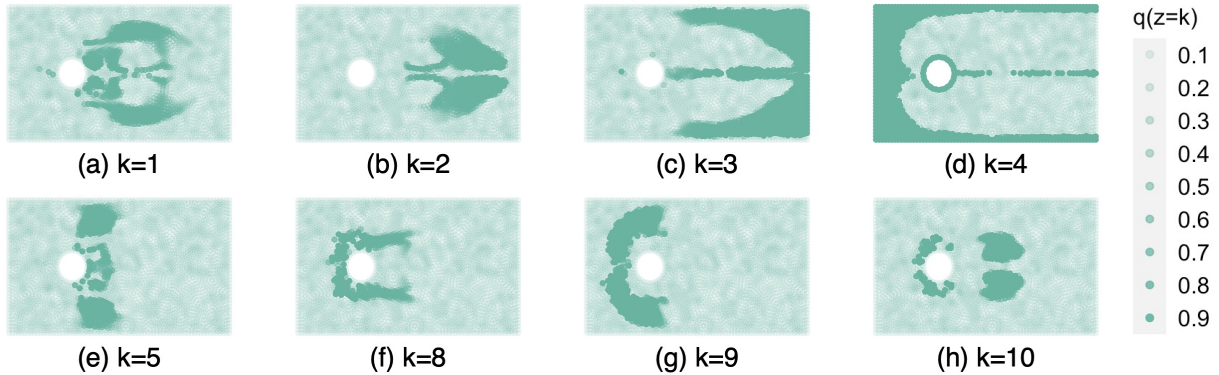


**Figure 10:** Variational distribution  $q(z_j = k)$  in the laminar flow application.

addition, the clusters  $k = 1, 2$ , and  $10$  have higher probability mass in the wake region. It turns out that the regions of high probability mass exerted by different clusters constitute the entire computational domain, implying the present clustering strategy is efficient.

The prediction and computation performance is examined on 100 uniformly random test input points from the input space. Three (out of 100) test FEM simulations along with the **mcGP** predictions are presented in Figure 11. From visual inspection, it appears that the point-wise predictions of **mcGP** are fairly accurate at the three input points. All dynamic structures in the flow are well captured, including the large-magnitude region in the front of the cylinder and the wake region behind the cylinder. Table 1 shows the results of the 100 test data in comparison of other GP models, indicating that the proposed **mcGP** outperforms the others in terms of prediction accuracy with reasonable computation time. Similar to the previous subsection, **pcaGP** performs the worst, which is not surprising because the approximation error of the dimension reduction approach can introduce additional bias to the predictions (Sung et al., 2022b). Unlike the previous subsection, **uGP** outperforms **iGP** in terms of both RMSE and CRPS. This again demonstrates that **mcGP** can serve as a middle ground between these two models.

### 5.3 Thermal stress analysis of jet engine turbine blade

In this subsection, we investigate the performance of the proposed method on a thermal stress analysis application for a jet turbine engine blade in steady-state operating condition. More details can be found in Wright and Han (2006), Carter (2005) and Sung et al. (2022a). In this study, we aim to emulate the thermal stress and deformation of a turbine with the



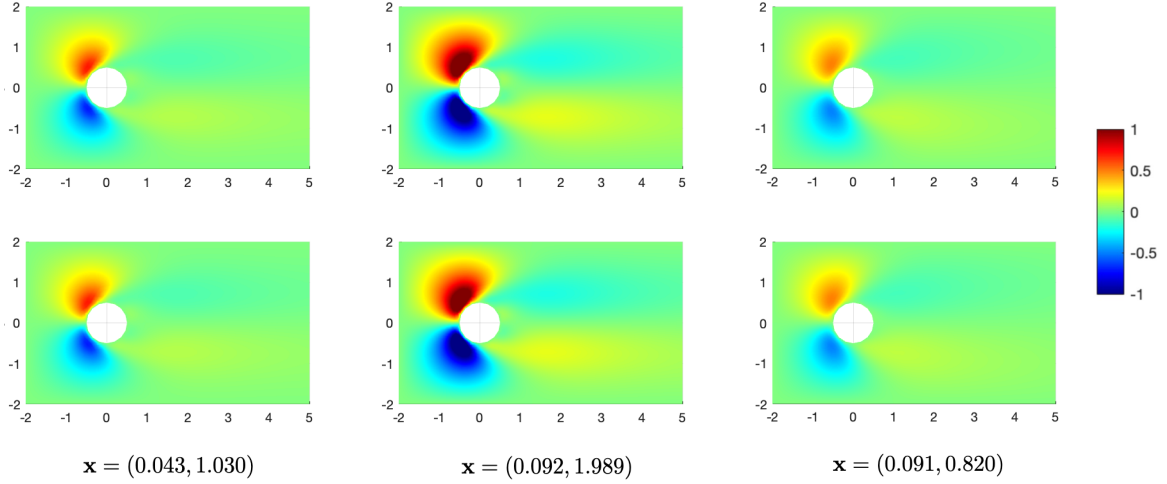


**Figure 11:** Validation performance of **mcGP** prediction in the laminar flow application. The upper panels present three (out of 100) test FEM simulations (with the input settings indicated by the values of  $\mathbf{x}$ ) and the bottom panels are the corresponding posterior means of **mcGP**.

method	mcGP	uGP	iGP	pcaGP
RMSE ( $\times 10^{-4}$ )	<b>8.741</b>	9.064	15.385	24.880
CRPS ( $\times 10^{-4}$ )	<b>2.276</b>	2.410	5.537	15.178
fitting time (sec.)	98	10	10	<b>0.13</b>
prediction time per run (msec.)	3	0.1	19	<b>0.06</b>

**Table 1:** Performance comparison in terms of prediction accuracy and computational cost in the laminar flow application, in which the better performances are boldfaced. Note that the test FEM simulations take, on average, 1068 milliseconds per run.

effect of the thermal stress and pressure of the surrounding gases on turbine blades. The problem is analyzed as a static structural model, which can be numerically solved using FEM. Two input variables are considered, which are the pressure load on the pressure ( $x_1$ ) and suction ( $x_2$ ) sides of the blade, both of which range from 0.25 to 0.75 MPa, i.e.,  $(x_1, x_2) \in [0.25, 0.75]^2$ . FEM simulations of sample size  $n = 30$  for the thermal stress are conducted via the Partial Differential Equation Toolbox (MATLAB, 2021). The sample points over the input space are allocated using the MaxPro design, which are presented in the left panel of Figure 12. The mesh size is set to 0.01, yielding  $N = 21158$  mesh nodes. Three (out of 30) training examples are presented in Figure 13. They show that larger suction pressure ( $x_2 = 0.60$  and  $0.69$ ) tends to impose higher thermal stress on the central

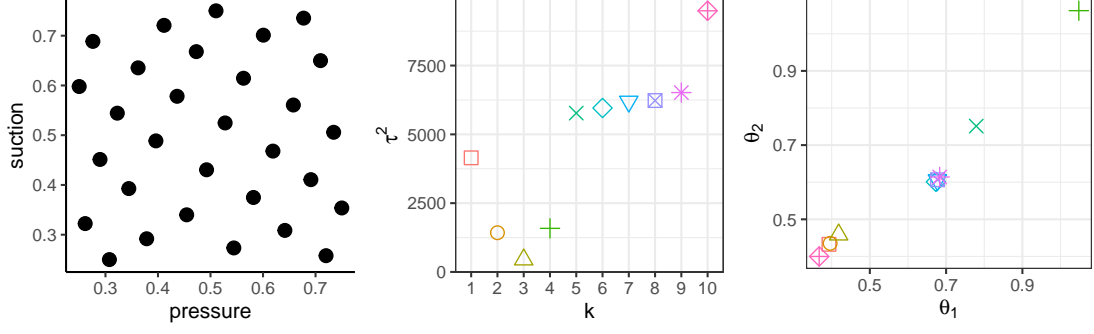


**Figure 12:** The left panel presents the design points in the turbine blade application, and the middle and right panels show the hyperparameter estimates of mcGP:  $\hat{\tau}_k$  (middle) and  $\hat{\theta}_k$  (right).

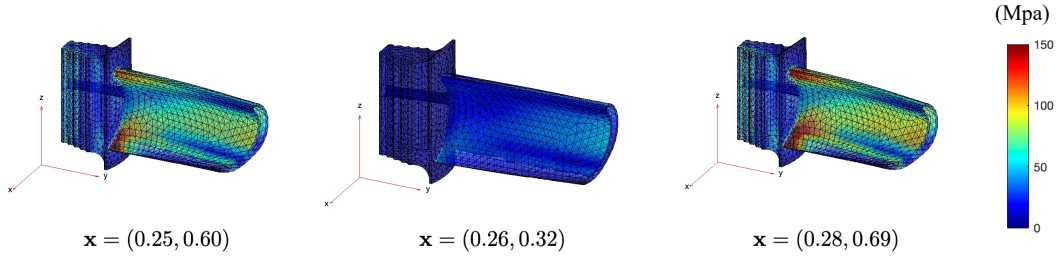


**Figure 13:** Three (out of 30) examples of the training FEM simulations in the turbine blade application, where the input settings are indicated by the values of  $\mathbf{x}$ .

area of the blade airfoil and the blade leading and trailing edges near the platform.

Figure 14 illustrates the variational distribution of the selected components,  $q(z_j = k)$ , and the corresponding hyperparameter estimates,  $\hat{\tau}_k^2$  and  $\hat{\theta}_k$ , are shown in the middle and right panels of Figure 12. The clusters  $k = 6, 7, 8$  and  $9$  are not shown here because  $q(z_j = k) < 0.3$  for all  $j$  at these clusters. The distribution of the nodes in resulting clusters correspond to the distribution of thermal stress in a physically meaning manner. The cluster  $k = 4$  has higher probability mass on the top center of the blade airfoil, where the thermal load is relatively large with high variability ( $\hat{\tau}_4^2 \approx 1584$ ) across different input settings; on the other hand, the cluster  $k = 3$  put higher probability mass on the platform area, where the thermal load is relatively small with subtle variability (small  $\hat{\tau}_3^2$ ). In addition, the cluster  $k = 1$  has higher probability mass on the leading and trailing edges of the blade next to the platform, which also tends to have a high variability ( $\tau^2 \approx 4147$ ) of the thermal stress.

Similar to Section 5.2, 100 test FEM simulations are conducted at uniformly random test input locations to examine the prediction and computation performance. Three (out of

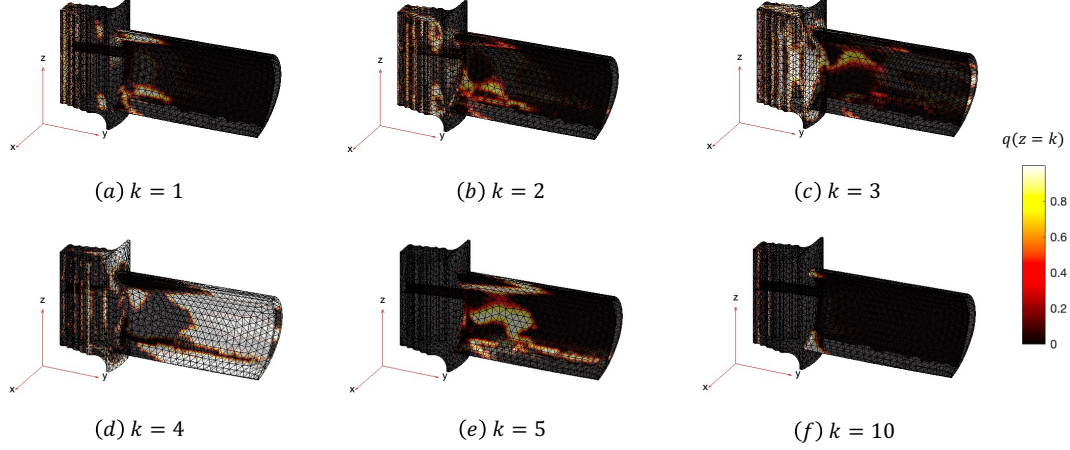


**Figure 14:** Variational distribution  $q(z_j = k)$  in the turbine blade application.

100) test examples are demonstrated in Figure 15, which shows that, from visual inspection, the predicted thermal stress (upper panels) closely mimics the simulated thermal stress (lower panels). In comparison with the competitors, the results are presented in Table 2, which again shows that the proposed method can outperform others in terms of prediction accuracy with reasonable computation time.

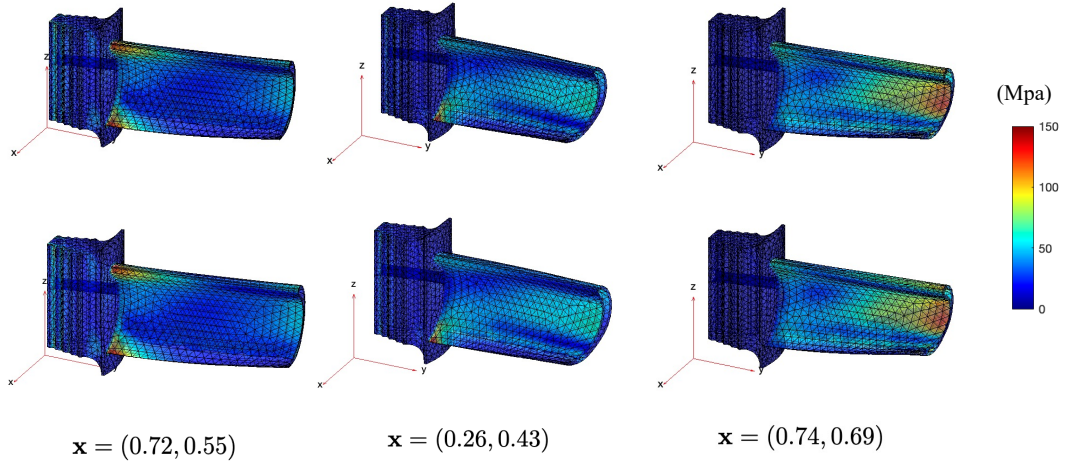


**Figure 15:** Validation performance of mcGP prediction in the turbine blade application. The upper panels present three (out of 100) test FEM simulations (with the input settings indicated by the values of  $\mathbf{x}$ ) and the bottom panels are the corresponding posterior means of mcGP.

method	mcGP	uGP	iGP	pcaGP
RMSE ( $\times 10^{-1}$ )	<b>9.800</b>	9.823	11.073	13.986
CRPS ( $\times 10^{-1}$ )	<b>3.204</b>	3.236	3.617	6.753
fitting time (sec.)	313	134	71	<b>0.19</b>
prediction time per run (msec.)	19	0.7	97	<b>0.3</b>

**Table 2:** Performance comparison in terms of prediction accuracy and computational cost in the turbine blade application, in which the better performances are boldfaced. Note that the test FEM simulations take, on average, 3819 milliseconds per run.

## 6 Concluding remarks

PDE simulations based on mesh-based numerical methods have become essential in various applications, ranging from engineering to health care. In this paper, we propose a new surrogate model for expensive PDE simulations that simultaneously emulates the simulation outputs across many mesh nodes. An important innovation of this work lies in its incorporation of mesh node locations into a statistical model, forming a mixture model that compromises the bias-variance trade-off in the context of many outputs. Furthermore, we develop a rigorous theoretical error analysis for the proposed emulator, which provides an important insight about its uncertainty quantification. Three real examples show that the method not only has advantages in prediction accuracy, but also enables discovery of interesting physics by interpreting the mixture clusters.

The proposed method shows several avenues for future research. First, in addition to the fine mesh in a spatial domain, the proposed method can be modified for simulations having fine grids over both the spatial and temporal domains. This can be naturally done by incorporating the time information into the latent model (13) to segment the temporal domain, and it is conceivable that the resulting clustering structures can reveal interesting *dynamic* features. Second, although the method developed herein assumes that the mesh specifications are identical across different input settings, the proposed method can be modified to tackle different mesh specifications. This can be done by utilizing the idea of *common grid* by Mak et al. (2018), which first identifies the densest grid among the training simulations and treats it as the common reference, and then interpolates output data onto this grid. This ensures the output data is realized over a common set of mesh nodes for all the training simulations. Lastly, it is worthwhile investigating the incorporation of the

boundary conditions into the proposed model as in Tan (2018a,b), to further improve the prediction accuracy. We leave these to our future work.

**Supplemental Materials** Additional supporting materials can be found in Supplemental Materials, including the detailed derivations for Algorithm 1, the derivation of (20), the detailed error analysis in Section 4, and the R code for reproducing the results in Section 5.

## References

- Akyildiz, Ö. D., Duffin, C., Sabanis, S., and Girolami, M. (2022). Statistical finite elements via Langevin dynamics. *SIAM/ASA Journal on Uncertainty Quantification*, 10(4):1560–1585.
- Arnold, D. N. (2012). Lecture notes on numerical analysis of partial differential equations.
- Bathe, K.-J. (2006). *Finite Element Procedures*. Klaus-Jurgen Bathe.
- Bishop, C. (2006). *Pattern Recognition and Machine Learning*. Springer New York.
- Blei, D. M. and Jordan, M. I. (2006). Variational inference for Dirichlet process mixtures. *Bayesian Analysis*, 1(1):121–143.
- Blei, D. M., Kucukelbir, A., and McAuliffe, J. D. (2017). Variational inference: A review for statisticians. *Journal of the American statistical Association*, 112(518):859–877.
- Bonilla, E. V., Chai, K., and Williams, C. (2007). Multi-task gaussian process prediction. In Platt, J., Koller, D., Singer, Y., and Roweis, S., editors, *Advances in Neural Information Processing Systems*, volume 20. Curran Associates, Inc.
- Brenner, S. C. (2008). *The mathematical theory of finite element methods*. Springer.
- Brenner, S. C. and Scott, L. R. (2007). *The Mathematical Theory of Finite Element Methods (Third Edition)*,. New York: Springer.
- Carter, T. J. (2005). Common failures in gas turbine blades. *Engineering Failure Analysis*, 12(2):237–247.

- Ciarlet, P. G. (2002). *The finite element method for elliptic problems*, volume 40. Siam.
- Conti, S. and O’Hagan, A. (2010). Bayesian emulation of complex multi-output and dynamic computer models. *Journal of statistical planning and inference*, 140(3):640–651.
- Cramér, H. and Leadbetter, M. R. (1967). *Stationary and Related Stochastic Processes: Sample Function Properties and Their Applications*. Courier Corporation.
- Dahl, A. and Bonilla, E. V. (2019). Grouped Gaussian processes for solar power prediction. *Machine Learning*, 108(8):1287–1306.
- Dancik, G. M. and Dorman, K. S. (2008). mlegp: statistical analysis for computer models of biological systems using r. *Bioinformatics*, 24(17):1966–1967.
- Duffin, C., Cripps, E., Stemler, T., and Girolami, M. (2021). Statistical finite elements for misspecified models. *Proceedings of the National Academy of Sciences*, 118(2):e2015006118.
- Evans, L. C. (2010). *Partial Differential Equations (Second Edition)*, volume 19. American Mathematical Society.
- Fasshauer, G. E. (1996). Solving partial differential equations by collocation with radial basis functions. In *Proceedings of Chamonix*, volume 1997, pages 1–8. Vanderbilt University Press Nashville, TN.
- Fasshauer, G. E. (1999). Solving differential equations with radial basis functions: multilevel methods and smoothing. *Advances in Computational Mathematics*, 11(2-3):139–159.
- Ferguson, T. S. (1973). A Bayesian analysis of some nonparametric problems. *The Annals of Statistics*, 1(2):209–230.
- Fornberg, B. and Flyer, N. (2015). Solving pdes with radial basis functions. *Acta Numerica*, 24:215–258.
- Fricker, T. E., Oakley, J. E., and Urban, N. M. (2013). Multivariate Gaussian process emulators with nonseparable covariance structures. *Technometrics*, 55(1):47–56.
- Ganguly, A. and Earp, S. W. (2021). An introduction to variational inference. *arXiv preprint arXiv:2108.13083*.

- Girolami, M., Febrianto, E., Yin, G., and Cirak, F. (2021). The statistical finite element method (statfem) for coherent synthesis of observation data and model predictions. *Computer Methods in Applied Mechanics and Engineering*, 375:113533.
- Gneiting, T. and Raftery, A. E. (2007). Strictly proper scoring rules, prediction, and estimation. *Journal of the American Statistical Association*, 102(477):359–378.
- Golberg, M., Chen, C., and Bowman, H. (1999). Some recent results and proposals for the use of radial basis functions in the bem. *Engineering Analysis with Boundary Elements*, 23(4):285–296.
- Gramacy, R. B. (2020). *Surrogates: Gaussian Process Modeling, Design, and Optimization for the Applied Sciences*. CRC Press.
- Grimit, E. P., Gneiting, T., Berrocal, V. J., and Johnson, N. A. (2006). The continuous ranked probability score for circular variables and its application to mesoscale forecast ensemble verification. *Quarterly Journal of the Royal Meteorological Society*, 132(621C):2925–2942.
- Gu, M., Berger, J. O., et al. (2016). Parallel partial gaussian process emulation for computer models with massive output. *The Annals of Applied Statistics*, 10(3):1317–1347.
- Higdon, D., Gattiker, J., Williams, B., and Rightley, M. (2008). Computer model calibration using high-dimensional output. *Journal of the American Statistical Association*, 103(482):570–583.
- Ishwaran, H. and James, L. F. (2001). Gibbs sampling methods for stick-breaking priors. *Journal of the American Statistical Association*, 96(453):161–173.
- Jordan, M. I., Ghahramani, Z., Jaakkola, T. S., and Saul, L. K. (1999). An introduction to variational methods for graphical models. *Machine Learning*, 37(2):183–233.
- Joseph, V. R., Gul, E., and Ba, S. (2015). Maximum projection designs for computer experiments. *Biometrika*, 102(2):371–380.
- Joseph, V. R. and Mak, S. (2021). Supervised compression of big data. *Statistical Analysis and Data Mining*, 14(3):217–229.

- Karhunen, K. (1947). *Ueber lineare Methoden in der Wahrscheinlichkeitsrechnung*, volume 37. Universitat Helsinki.
- Kleijnen, J. P. C. and Mehdad, E. (2014). Multivariate versus univariate kriging meta-models for multi-response simulation models. *European Journal of Operational Research*, 236(2):573–582.
- Lee, L., Carslaw, K., Pringle, K., and Mann, G. (2012). Mapping the uncertainty in global ccn using emulation. *Atmospheric Chemistry and Physics*, 12(20):9739–9751.
- Lee, L., Carslaw, K., Pringle, K., Mann, G., and Spracklen, D. (2011). Emulation of a complex global aerosol model to quantify sensitivity to uncertain parameters. *Atmospheric Chemistry and Physics*, 11(23):12253–12273.
- Li, M., Liu, M.-Q., Wang, X.-L., and Zhou, Y.-D. (2020). Prediction for computer experiments with both quantitative and qualitative factors. *Statistics & Probability Letters*, page 108858.
- Lo, A. Y. (1984). On a class of Bayesian nonparametric estimates: I. density estimates. *The Annals of Statistics*, 12(1):351–357.
- Loève, M. (1955). *Probability Theory: Foundations, Random Sequences*. New York: D. Van Nostrand Company.
- Ltd., Q. (2022). QuickerSim CFD Toolbox. <https://old.quickersim.com/cfdtoolbox/>. [Online; accessed 10-November-2022].
- Lumley, J. L. (1967). The structure of inhomogeneous turbulent flows. *Atmospheric Turbulence and Radio Wave Propagation*, pages 166–178.
- Mak, S., Sung, C.-L., Wang, X., Yeh, S.-T., Chang, Y.-H., Joseph, V. R., Yang, V., and Wu, C. F. J. (2018). An efficient surrogate model for emulation and physics extraction of large eddy simulations. *Journal of the American Statistical Association*, 113(524):1443–1456.
- Marrel, A., Iooss, B., Jullien, M., Laurent, B., and Volkova, E. (2011). Global sensitivity analysis for models with spatially dependent outputs. *Environmetrics*, 22(3):383–397.



- MATLAB (2021). *MATLAB version 9.11.0.1769968 (R2021b)*. The Mathworks, Inc., Natick, Massachusetts.
- Meeds, E. and Osindero, S. (2005). An alternative infinite mixture of Gaussian process experts. *Advances in Neural Information Processing systems*, 18.
- Neal, R. M. (1992). Bayesian mixture modeling. In *Maximum Entropy and Bayesian Methods*, volume 11, pages 197–211. Springer.
- Neal, R. M. (2000). Markov chain sampling methods for Dirichlet process mixture models. *Journal of Computational and Graphical Statistics*, 9(2):249–265.
- Ng, A. and Jordan, M. (2001). On discriminative vs. generative classifiers: A comparison of logistic regression and naive bayes. *Advances in Neural Information Processing Systems*, 14.
- Qian, P. Z. G., Wu, H., and Wu, C. F. J. (2008). Gaussian process models for computer experiments with qualitative and quantitative factors. *Technometrics*, 50(3):383–396.
- R Core Team (2018). *R: A Language and Environment for Statistical Computing*. R Foundation for Statistical Computing, Vienna, Austria.
- Rajani, B. N., Kandasamy, A., and Majumdar, S. (2009). Numerical simulation of laminar flow past a circular cylinder. *Applied Mathematical Modelling*, 33(3):1228–1247.
- Ramsay, J. O. and Silverman, B. W. (2005). *Functional Data Analysis (Second Edition)*. Springer New York, NY.
- Rasmussen, C. (2000). The infinite Gaussian mixture model. *Advances in Neural Information Processing systems*, 12.
- Rasmussen, C. and Ghahramani, Z. (2001). Infinite mixtures of Gaussian process experts. *Advances in Neural Information Processing Systems*, 14.
- Rougier, J. (2008). Efficient emulators for multivariate deterministic functions. *Journal of Computational and Graphical Statistics*, 17(4):827–843.

- Rougier, J., Guillas, S., Maute, A., and Richmond, A. D. (2009). Expert knowledge and multivariate emulation: The thermosphere–ionosphere electrodynamics general circulation model (tie-gcm). *Technometrics*, 51(4):414–424.
- Santner, T. J., Williams, B. J., and Notz, W. I. (2018). *The Design and Analysis of Computer Experiments*. Springer Science & Business Media.
- Seo, I. W. and Song, C. G. (2012). Numerical simulation of laminar flow past a circular cylinder with slip conditions. *International Journal for Numerical Methods in Fluids*, 68(12):1538–1560.
- Sethuraman, J. (1994). A constructive definition of Dirichlet priors. *Statistica Sinica*, 4(2):639–650.
- Stein, M. L. (1999). *Interpolation of Spatial Data: Some Theory for Kriging*. Springer Science & Business Media.
- Sun, S. and Xu, X. (2010). Variational inference for infinite mixtures of Gaussian processes with applications to traffic flow prediction. *IEEE Transactions on Intelligent Transportation Systems*, 12(2):466–475.
- Sung, C.-L., Haaland, B., Hwang, Y., and Lu, S. (2023). A clustered Gaussian process model for computer experiments. *Statistica Sinica*. To appear.
- Sung, C.-L., Hung, Y., Rittase, W., Zhu, C., and Wu, C. F. J. (2020). Calibration for computer experiments with binary responses and application to cell adhesion study. *Journal of the American Statistical Association*, 115(532):1664–1674.
- Sung, C.-L., Ji, Y., Tang, T., and Mak, S. (2022a). Stacking designs: designing multi-fidelity computer experiments with confidence. *arXiv preprint arXiv:2211.00268*.
- Sung, C.-L., Wang, W., Cakoni, F., Harris, I., and Hung, Y. (2022b). Functional-input gaussian processes with applications to inverse scattering problems. *Statistica Sinica*. To appear.
- Svenson, J. and Santner, T. (2016). Multiobjective optimization of expensive-to-evaluate deterministic computer simulator models. *Computational Statistics & Data Analysis*, 94(1):250–264.

- Tan, M. H. (2018a). Gaussian process modeling of a functional output with information from boundary and initial conditions and analytical approximations. *Technometrics*, 60(2):209–221.
- Tan, M. H. Y. (2018b). Gaussian process modeling with boundary information. *Statistica Sinica*, 28(2):621–648.
- Tekkaya, A. E. and Soyarslan, C. (2019). Finite element method. In Chatti, S., Laperrière, L., Reinhart, G., and Tolio, T., editors, *CIRP Encyclopedia of Production Engineering*, pages 677–683. Springer Berlin Heidelberg.
- Tuo, R., Wu, C. F. J., and Yu, D. (2014). Surrogate modeling of computer experiments with different mesh densities. *Technometrics*, 56(3):372–380.
- Wainwright, M. J. and Jordan, M. I. (2008). Graphical models, exponential families, and variational inference. *Foundations and Trends® in Machine Learning*, 1(1–2):1–305.
- Wang, J.-L., Chiou, J.-M., and Müller, H.-G. (2016). Functional data analysis. *Annual Review of Statistics and Its Application*, 3:257–295.
- Wang, Y., Wang, X., and Yang, V. (2018). Evolution and transition mechanisms of internal swirling flows with tangential entry. *Physics of Fluids*, 30(1):013601.
- Wendland, H. (1998). Numerical solution of variational problems by radial basis functions. *Approximation Theory IX*, 2:361–368.
- Wendland, H. (1999). Meshless galerkin methods using radial basis functions. *Mathematics of Computation of the American Mathematical Society*, 68(228):1521–1531.
- Wendland, H. (2004). *Scattered Data Approximation*, volume 17. Cambridge University Press.
- Wilson, A. G., Knowles, D. A., and Ghahramani, Z. (2012). Gaussian process regression networks. In *International Conference on Machine Learning*.
- Wright, L. M. and Han, J.-C. (2006). Enhanced internal cooling of turbine blades and vanes. *The Gas Turbine Handbook*, 4:1–5.

- Wu, Z. and Schaback, R. (1993). Local error estimates for radial basis function interpolation of scattered data. *IMA Journal of Numerical Analysis*, 13(1):13–27.
- Yuan, C. and Neubauer, C. (2009). Variational mixture of Gaussian process experts. *Advances in Neural Information Processing Systems*, 21:1897–1904.
- Zhang, H. and Cai, W. (2015). When doesn’t cokriging outperform kriging? *Statistical Science*, 30(2):176–180.

# Supplementary Materials for “Mesh-clustered Gaussian process emulator for partial differential equation systems”

## S1 Detailed derivations for the variational expectation maximization algorithm

In this section, the detailed derivations for Algorithm 1, including the optimal variational distributions, the estimators in the M-step, and the ELBO, are presented.

The optimal variational distribution for each  $\omega \in \phi$  can be obtained by

$$\log q(\omega) = \mathbb{E}_{\phi \setminus \omega}[\log p(\mathbf{D}, \phi)] + \text{constant}.$$

The following derivations are developed along the lines described in Sun and Xu (2010). In particular, the derivations for  $q(\boldsymbol{\mu}_k)$  and  $q(\boldsymbol{\Sigma}_k)$  can be found in Sun and Xu (2010). For  $q(z_j = k)$ , we have

$$\begin{aligned} \log q(z_j) &= \mathbb{E}_{\phi \setminus z_j}[\log p(\mathbf{D}, \phi)] + \text{constant} \\ &= \mathbb{E}_{\phi \setminus z_j}[\log p(\mathbf{b}_j | z_j) + \log p(\mathbf{s}_j | z_j, \tilde{\boldsymbol{\mu}}, \tilde{\boldsymbol{\Sigma}}) + \log p(z_j | \tilde{\boldsymbol{\gamma}})] + \text{constant}. \end{aligned} \quad (\text{S1.1})$$

Since  $\mathbf{b}_j | z_j = k \sim \mathcal{N}_n(0, \tau_k^2 \Phi_{\boldsymbol{\theta}_k}(\mathbf{X}_n, \mathbf{X}_n))$  (see (9)), we have

$$\mathbb{E}_{\phi \setminus z_j}[\log p(\mathbf{b}_j | z_j)] = \sum_{k=1}^{\infty} \mathbb{1}(z_j = k) \mathbb{E}_q[\log p(\mathbf{b}_j | z_j = k)] = \frac{1}{2} \sum_{k=1}^{\infty} \mathbb{1}(z_j = k) t_{jk} \quad (\text{S1.2})$$

with

$$t_{jk} = -\log \tau_k^2 - \log |\Phi_{\boldsymbol{\theta}_k}(\mathbf{X}_n, \mathbf{X}_n)| - \frac{1}{\tau_k^2} (\mathbf{b}_j^T \Phi_{\boldsymbol{\theta}_k}(\mathbf{X}_n, \mathbf{X}_n)^{-1} \mathbf{b}_j) - n \log 2\pi.$$

Since  $\mathbf{s}_j | z_j = k \sim \mathcal{N}_d(\boldsymbol{\mu}_k, \boldsymbol{\Sigma}_k^{-1})$  (see (13)), we have

$$\mathbb{E}_{\phi \setminus z_j}[\log p(\mathbf{s}_j | z_j, \tilde{\boldsymbol{\mu}}, \tilde{\boldsymbol{\Sigma}})] = \sum_{k=1}^{\infty} \mathbb{1}(z_j = k) \mathbb{E}_q[\log p(\mathbf{s}_j | z_j = k, \tilde{\boldsymbol{\mu}}, \tilde{\boldsymbol{\Sigma}})] = \frac{1}{2} \sum_{k=1}^{\infty} \mathbb{1}(z_j = k) s_{jk} \quad (\text{S1.3})$$

with

$$s_{jk} = \mathbb{E}_q[\log |\Sigma_k|] - \mathbb{E}_q[(\mathbf{s}_j - \boldsymbol{\mu}_k)^T \Sigma_k (\mathbf{s}_j - \boldsymbol{\mu}_k)] - d \log 2\pi.$$

For the expectation,  $\mathbb{E}_{\phi \setminus z_j}[\log p(z_j | \tilde{\gamma})]$ , we follow expression in Blei and Jordan (2006); Sun and Xu (2010), which gives

$$\mathbb{E}_{\phi \setminus z_j}[\log p(z_j | \tilde{\gamma})] = \sum_{k=1}^{\infty} (\mathbb{1}(z_j > k) \mathbb{E}_q[\log(1 - \gamma_k)] + \mathbb{1}(z_j = k) \mathbb{E}_q[\log \gamma_k]). \quad (\text{S1.4})$$

Together with (S1.1), (S1.2), (S1.3), (S1.4), and by the fact that  $q(z_j > K) = 0$ , we have

$$\log q(z_j = k) = \frac{1}{2}(s_{jk} + t_{jk}) + \mathbb{E}_q[\log \gamma_k] + \sum_{i=1}^{k-1} \mathbb{E}_q[\log(1 - \gamma_i)],$$

which gives the variational distribution  $q(z_j = k)$  as in Algorithm 1.

We now derive the hyperparameter estimates of  $\boldsymbol{\theta}_k$  and  $\tau_k^2$  in the M-step. We first optimize  $\mathbb{E}_q[\log p(\mathbf{D}, \boldsymbol{\phi})]$  as in (18) with respect to  $\tau_k^2$ . This can be done by taking the derivative with respect to  $\tau_k^2$ ,

$$\frac{\partial \mathbb{E}_q[\log p(\mathbf{D}, \boldsymbol{\phi})]}{\partial \tau_k^2} = -\frac{1}{2} \sum_{j=1}^N \left( n \frac{q(z_j = k)}{\tau_k^2} - \frac{q(z_j = k)}{(\tau_k^2)^2} \mathbf{b}_j^T \Phi_{\boldsymbol{\theta}_k}(\mathbf{X}_n, \mathbf{X}_n)^{-1} \mathbf{b}_j \right),$$

which gives

$$\hat{\tau}_k^2 = \frac{\sum_{j=1}^N q(z_j = k) \mathbf{b}_j^T \Phi_{\boldsymbol{\theta}_k}(\mathbf{X}_n, \mathbf{X}_n)^{-1} \mathbf{b}_j}{n \sum_{j=1}^N q(z_j = k)}.$$

By plugging  $\hat{\tau}_k^2$  into (18), it follows that

$$\begin{aligned} & \text{constant} - \frac{1}{2} \sum_{j=1}^N \sum_{k=1}^K q(z_j = k) \times \\ & \left( \log |\Phi_{\boldsymbol{\theta}_k}(\mathbf{X}_n, \mathbf{X}_n)| + n \log \sum_{j'=1}^N q(z_{j'} = k) \mathbf{b}_{j'}^T \Phi_{\boldsymbol{\theta}_k}(\mathbf{X}_n, \mathbf{X}_n)^{-1} \mathbf{b}_{j'} - n \log \left( n \sum_{j'=1}^N q(z_{j'} = k) \right) \right). \end{aligned} \quad (\text{S1.5})$$

Thus, maximizing the above objective function with respect to  $\hat{\boldsymbol{\theta}}_k$  is equivalent to

$$\hat{\boldsymbol{\theta}}_k = \underset{\boldsymbol{\theta}_k}{\operatorname{argmin}} \left( \log |\Phi_{\boldsymbol{\theta}_k}(\mathbf{X}_n, \mathbf{X}_n)| + n \log \sum_{j=1}^N q(z_j = k) \mathbf{b}_j^T \Phi_{\boldsymbol{\theta}_k}(\mathbf{X}_n, \mathbf{X}_n)^{-1} \mathbf{b}_j \right).$$

Lastly, we derive the evidence lower bound (ELBO) as follows. The ELBO can be written as

$$\begin{aligned} \text{ELBO} &= \mathbb{E}_q[\log p(\mathbf{D}, \boldsymbol{\phi})] - \\ &\quad \sum_{k=1}^{K-1} |\mathbb{E}_q[\log(q(\gamma_k))]| - \sum_{k=1}^K \mathbb{E}_q[\log(q(\boldsymbol{\mu}_k))]| - \sum_{k=1}^K \mathbb{E}_q[\log(q(\boldsymbol{\Sigma}_k))]| - \sum_{j=1}^N \mathbb{E}_q[\log(q(z_j))]| \\ &:= A + B + C + D + E, \end{aligned}$$

where the derivations for  $A, B, C, D$ , and  $E$  are given below.

For  $A := \mathbb{E}_q[\log p(\mathbf{D}, \boldsymbol{\phi})]$ , it has the form of (S1.5). For  $B := -\sum_{k=1}^{K-1} |\mathbb{E}_q[\log(q(\gamma_k))]|$ , since  $q(\gamma_k) \sim \text{Beta}(a_k, b_k)$ , we have

$$B = \sum_{k=1}^{K-1} (\log B(a_k, b_k) - (a_k - 1)\psi(a_k) - (b_k - 1)\psi(b_k) + (a_k + b_k - 2)\psi(a_k + b_k)),$$

where  $B$  is the beta function defined as  $B(\alpha, \beta) = \Gamma(\alpha)\Gamma(\beta)/\Gamma(\alpha + \beta)$ , and  $\psi$  is the digamma function defined as  $\psi(\alpha) = d \log(\Gamma)/d\alpha$ .

For  $C := -\sum_{k=1}^K |\mathbb{E}_q[\log(q(\boldsymbol{\mu}_k))]|$ , since  $q(\gamma_k) \sim \mathcal{N}_d((\boldsymbol{\Sigma}_0 + \mathbf{R}_{k2})^{-1}(\boldsymbol{\Sigma}_0 \boldsymbol{\mu}_0 + \mathbf{R}_{k1}), (\boldsymbol{\Sigma}_0 + \mathbf{R}_{k2})^{-1})$ , we have

$$C = \sum_{k=1}^K \frac{1}{2} (d \log(2\pi) + d - \log(|\boldsymbol{\Sigma}_0 + \mathbf{R}_{k2}|)).$$

For  $D := -\sum_{k=1}^K |\mathbb{E}_q[\log(q(\boldsymbol{\Sigma}_k))]|$ , since  $\boldsymbol{\Sigma}_k \sim \mathcal{W}(\mathbf{W}_k, \kappa_k)$ , we have

$$D = \sum_{k=1}^K \left( \frac{d+1}{2} \log |\mathbf{W}_k| + \frac{\log 2}{2} d(d+1) + \log \Gamma_d \left( \frac{\kappa_k}{2} \right) - \frac{\kappa_k - d - 1}{2} \psi_d \left( \frac{\kappa_k}{2} \right) + \frac{d\kappa_k}{2} \right),$$

where  $\psi_d$  is the is the multivariate digamma function and  $\Gamma_d$  is the multivariate gamma

function defined as

$$\Gamma_d\left(\frac{\kappa}{2}\right) = \pi^{d(d-1)/4} \prod_{j=1}^d \Gamma\left(\frac{\kappa}{2} - \frac{j-1}{2}\right).$$

For  $E := -\sum_{j=1}^N |\mathbb{E}_q[\log(q(z_j))]|$ , since  $q(z_j)$  is a categorical distribution with the probability  $p_{jk} := q(z_j = k) = r_{jk} / \sum_{k=1}^K r_{jk}$ , we have

$$E = -\sum_{j=1}^N \sum_{k=1}^K p_{jk} \log(p_{jk}).$$

## S2 Derivation of (20)

For notational simplicity, we denote  $\mathcal{D} = \{\mathbf{D}, \{\hat{\boldsymbol{\theta}}_k, \hat{\tau}_k^2\}_{k=1}^K\}$ . Since the conditional distributions  $\{\beta_j(\mathbf{x})|z_j\}_{j=1}^N$  are independent and the variational distributions  $\{q(z_j)\}_{j=1}^N$  are independent, the distribution  $\beta_j(\mathbf{x})$  is mutually independent for  $j = 1, \dots, N$ . Thus, the variance of  $u_N(\mathbf{s}, \mathbf{x})$  conditioned on  $\mathcal{D}$  can be expressed as:

$$\mathbb{V}[u_N(\mathbf{s}, \mathbf{x})|\mathcal{D}] = \mathbb{V}\left[\sum_{j=1}^N \beta_j(\mathbf{x})v_j(\mathbf{s})|\mathcal{D}\right] = \sum_{j=1}^N \mathbb{V}[\beta_j(\mathbf{x})|\mathcal{D}]v_j(\mathbf{s})^2.$$

The term  $\mathbb{V}[\beta_j(\mathbf{x})|\mathcal{D}]$  can be obtained as follows:

$$\begin{aligned} \mathbb{V}[\beta_j(\mathbf{x})|\mathcal{D}] &= \mathbb{E}[\mathbb{V}[\beta_j(\mathbf{x})|z_j, \mathcal{D}]] + \mathbb{V}[\mathbb{E}[\beta_j(\mathbf{x})|z_j, \mathcal{D}]] \\ &= \mathbb{E}[\mathbb{V}[\beta_j(\mathbf{x})|z_j, \mathcal{D}]] + \mathbb{E}[(\mathbb{E}[\beta_j(\mathbf{x})|z_j, \mathcal{D}])^2] - (\mathbb{E}[\mathbb{E}[\beta_j(\mathbf{x})|z_j, \mathcal{D}]])^2. \end{aligned}$$

By (6), the first term follows that

$$\begin{aligned} \mathbb{E}[\mathbb{V}[\beta_j(\mathbf{x})|z_j, \mathcal{D}]] &= \mathbb{E}[\hat{\tau}_{z_j}^2 (1 - \Gamma_{\hat{\boldsymbol{\theta}}_{z_j}}(\mathbf{x}, \mathbf{X}_n) \Phi_{\hat{\boldsymbol{\theta}}_{z_j}}(\mathbf{x}, \mathbf{X}_n)^T)] \\ &= \sum_{k=1}^K q(z_j = k) \hat{\tau}_k^2 (1 - \Gamma_{\hat{\boldsymbol{\theta}}_k}(\mathbf{x}, \mathbf{X}_n) \Phi_{\hat{\boldsymbol{\theta}}_k}(\mathbf{x}, \mathbf{X}_n)^T), \end{aligned}$$

and by (5), the second and third terms follow that

$$\mathbb{E}[(\mathbb{E}[\beta_j(\mathbf{x})|z_j, \mathcal{D}])^2] = \mathbb{E}[(\Gamma_{\hat{\boldsymbol{\theta}}_{z_j}}(\mathbf{x}, \mathbf{X}_n) \mathbf{b}_j)^2] = \sum_{k=1}^K q(z_j = k) (\Gamma_{\hat{\boldsymbol{\theta}}_k}(\mathbf{x}, \mathbf{X}_n) \mathbf{b}_j)^2$$



and

$$(\mathbb{E}[\mathbb{E}[\beta_j(\mathbf{x})|z_j, \mathcal{D}]])^2 = \left( \sum_{k=1}^K q(z_j = k) \Gamma_{\hat{\theta}_k}(\mathbf{x}, \mathbf{X}_n) \mathbf{b}_j \right)^2,$$

respectively. This finishes the derivation of (20).

### S3 Simulation error

Here we focus on the simulation error based on FEM simulations, which are widely used in practice and have extensive studies in literature (Arnold, 2012; Brenner and Scott, 2007). In this subsection we briefly review the analysis results of the simulation error by FEM.

Suppose that  $\Omega$  is triangulated by the FEM with  $N$  mesh nodes and let  $\mathcal{T}_N$  be this triangulation. See Figure 1 as an example and we refer detailed discussions of the triangulation to Ciarlet (2002). Let  $H^r(\Omega)$  denote the Sobolev space defined by

$$H^r(\Omega) = \{f \in L_2(\Omega) : D^\alpha f \in L_2(\Omega), \forall |\alpha| \leq r\}$$

with  $r > 0$ , where  $D^\alpha f$  is the weak  $\alpha$ -th partial derivative of  $f$ . Table 3 lists the upper bounds of the simulation errors by FEM for some common PDE systems. It can be seen that in these systems, for any  $\mathbf{x} \in \chi$ , the  $L_2$  error typically has the form

$$\|u_0(\cdot, \mathbf{x}) - u_N(\cdot, \mathbf{x})\|_{L_2(\Omega)} \leq C(\mathbf{x}) h_{\mathcal{T}_N}^{r_1} \|u_0(\cdot, \mathbf{x})\|_{H^{r_2}(\Omega)}, \quad (\text{S3.6})$$

where positive integers  $r_1$  and  $r_2$  are dependent on each other, and  $r_1$  is also related to the degree of the shape function,  $C(\mathbf{x})$  is constant dependent on  $\mathbf{x}$ , and  $h_{\mathcal{T}_N}$  is the *mesh size* of  $\mathcal{T}_N$ , which is the size of the elements used to triangulate the domain  $\Omega$  (Brenner, 2008). The smaller the mesh size, the more elements are used to cover the region, resulting in a more accurate solution, but at the cost of increased computational time. Since  $\chi$  is compact and convex, the error (S3.6) can reduce to

$$\|u_0 - u_N\|_{L_2(\Omega, \chi)} \leq C_\chi h_{\mathcal{T}_N}^{r_1} \sup_{\mathbf{x} \in \chi} \|u_0(\cdot, \mathbf{x})\|_{H^{r_2}(\Omega)} \quad (\text{S3.7})$$

PDE system	Boundary conditions	Error bounds
Poisson's equation	Dirichlet boundary condition: $u = 0$ on $\partial\Omega$	$C(\mathbf{x})h_{\mathcal{T}_h}^{r+1}\ u(\cdot, \mathbf{x})\ _{H^{r+1}(\Omega)}$
	Neumann boundary condition: $\frac{\partial u}{\partial \mathbf{n}} = 0$ on $\partial\Omega$	$C(\mathbf{x})h_{\mathcal{T}_h}^r\ u(\cdot, \mathbf{x})\ _{H^{r+1}(\Omega)}$
Biharmonic problem	$u = \frac{\partial u}{\partial \mathbf{n}} = 0$ on $\partial\Omega$	$C(\mathbf{x})h_{\mathcal{T}_h}^4\ u(\cdot, \mathbf{x})\ _{H^6(\Omega)}$
Hyperbolic problems	$u_0 = f$ in $\Omega$ and $u = g$ on $\partial\Omega$	$C(\mathbf{x})h_{\mathcal{T}_h}^{r+1}\ u(\cdot, \mathbf{x})\ _{H^{r+1}(\Omega)}$

**Table 3:** Error bounds of finite element methods for different PDE systems, where  $\frac{\partial}{\partial \mathbf{n}}$  is the outward normal derivative on  $\partial\Omega$  and  $h_{\mathcal{T}_h}$  is the mesh size of  $\mathcal{T}_h$ .

with  $C_\chi = \text{Vol}(\chi) \sup_{\mathbf{x} \in \chi} C(\mathbf{x})$  where  $\text{Vol}(\chi)$  is the volume of  $\chi$ . According to equation (4.5.19) in Brenner and Scott (2007),  $h_{\mathcal{T}_N} \leq CN^{-1/d}$  for some constant  $C$  independent of  $h_{\mathcal{T}_N}$  if the triangulation  $\mathcal{T}_N$  is quasi-uniform, i.e., there exists some  $\rho > 0$  s.t.  $\min_{T \in \mathcal{T}_N} \{\text{diam}(T)\} \geq \rho h_{\mathcal{T}_N} \text{diam}(\chi)$ , where  $d$  is the dimension of the space  $\Omega$ . Quasi-uniform triangulation includes the most commonly used Delaunay Triangulation. This shows that with this triangulation, the simulation error decreases at the rate  $r_1/d$  with increasing  $N$ .

## S4 Emulation error

In this section, we assume that  $\hat{\boldsymbol{\theta}}_k$  is fixed and known, and  $\Phi_{\hat{\boldsymbol{\theta}}_k}$  is suppressed by  $\Phi_k$  for notational convenience. By the triangle inequality, the emulation error can be bounded by

$$|u_N(\mathbf{s}, \mathbf{x}) - \hat{u}_N(\mathbf{s}, \mathbf{x})| \leq \sum_{j=1}^N \left| \beta_j(\mathbf{x}) - \sum_{k=1}^K q_{jk} \Phi_k(\mathbf{x}, \mathbf{X}_n) \Phi_k(\mathbf{X}_n, \mathbf{X}_n)^{-1} \mathbf{b}_j \right| v_j(\mathbf{s}). \quad (\text{S4.8})$$

Denote  $\mathcal{N}_\Phi(\chi)$  as a *reproducing kernel Hilbert space (RKHS)* associated with a particular kernel  $\Phi$ , and the corresponding norm is denoted by  $\|\beta\|_{\mathcal{N}_\Phi(\chi)}$  for a function  $\beta(\mathbf{x}) \in \mathcal{N}_\Phi(\chi)$  (Wendland, 2004). The upper bound of the emulation error (S4.8) can be obtained in the following theorem. We first denote  $h_{\mathbf{X}_n}$  as the *fill distance* of  $\mathbf{X}_n$ , i.e.,

$$h_{\mathbf{X}_n} := \sup_{\mathbf{x} \in \chi} \min_{\mathbf{x}_i \in \mathbf{X}_n} \|\mathbf{x} - \mathbf{x}_i\|_2.$$

**Theorem S4.1.** *Let  $\chi$  be compact and convex with a positive Lebesgue measure and  $\Phi_k$  be a Matérn kernel as in (7) with the smoothness parameter  $\nu$ . Suppose that  $\beta_j(\mathbf{x}) \in \bigcup_{k=1, \dots, K} \mathcal{N}_{\Phi_k}(\chi)$ . Then, provided that  $h_{\mathbf{X}_n} \leq h_0$  for a constant  $h_0$ , there exists a constant*

$C_\chi$  (dependent of  $\chi$ ) such that

$$\|u_N - \hat{u}_N\|_{L_2(\Omega, \chi)} \leq C_\chi h_{\mathbf{X}_n}^\nu \max_{j \leq N; k \leq K} (\|\beta_j\|_{\mathcal{N}_{\Phi_k(\chi)}} \|v_j\|_{L_\infty(\Omega)}). \quad (\text{S4.9})$$

*Proof.* Without loss of generality, let  $\Phi(\mathbf{x}, \mathbf{x}) = 1$  for all  $\mathbf{x} \in \chi$ . We first introduce the RKHS interpolator and its property. The RKHS interpolator of  $\beta$  given the data  $\mathbf{b} = (\beta(\mathbf{x}_1), \dots, \beta(\mathbf{x}_n))$ , associated with the kernel  $\Phi$ , has the form

$$\mathcal{I}_{\Phi, \mathbf{X}_n} \beta(\mathbf{x}) = \Phi(\mathbf{x}, \mathbf{X}_n) \Phi(\mathbf{X}_n, \mathbf{X}_n)^{-1} \mathbf{b},$$

where the interpolation operator  $\mathcal{I}_{\Phi, \mathbf{X}_n}$  is also called *radial basis function approximation*. For  $\beta \in \mathcal{N}_\Phi(\chi)$ , a pointwise error bound for the RKHS interpolator (Wendland (2004), Theorem 11.4) is given by:

$$|\beta(\mathbf{x}) - \mathcal{I}_{\Phi, \mathbf{X}_n} \beta(\mathbf{x})| \leq P_{\Phi, \mathbf{X}_n}(\mathbf{x}) \|\beta\|_{\mathcal{N}_{\Phi(\chi)}}, \quad (\text{S4.10})$$

where  $P_{\Phi, \mathbf{X}_n}^2(\mathbf{x}) = 1 - \Phi(\mathbf{x}, \mathbf{X}_n) \Phi(\mathbf{X}_n, \mathbf{X}_n)^{-1} \Phi(\mathbf{x}, \mathbf{X}_n)^T$  which is called the *power function*. Then, by Theorem 5.14 in Wu and Schaback (1993), there exist constants  $h_0$  and  $C_\chi$  which is only dependent on  $\chi$ , such that

$$P_{\Phi, \mathbf{X}_n}(\mathbf{x}) \leq C_\chi h_{\mathbf{X}_n}^\nu \quad (\text{S4.11})$$

provided that  $h_{\mathbf{X}_n} \leq h_0$ , where  $h_{\mathbf{X}_n}$  is the fill distance of  $\mathbf{X}_n$ .

For notational simplicity, let  $q_{jk} := q(z_j = k)$ . By (S4.8), (S4.10), (S4.11), and the

triangle inequality, it follows that

$$\begin{aligned}
|u_N(\mathbf{s}, \mathbf{x}) - \hat{u}_N(\mathbf{s}, \mathbf{x})| &\leq \sum_{j=1}^N \left| \beta_j(\mathbf{x}) - \sum_{k=1}^K q_{jk} \Phi_k(\mathbf{x}, \mathbf{X}_n) \Phi_k(\mathbf{X}_n, \mathbf{X}_n)^{-1} \mathbf{b}_j \right| v_j(\mathbf{s}) \\
&\leq \sum_{j=1}^N \left| \sum_{k=1}^K q_{jk} (\beta_j(\mathbf{x}) - \mathcal{I}_{\Phi_k, \mathbf{X}_n} \beta_j(\mathbf{x})) \right| v_j(\mathbf{s}) \\
&\leq \sum_{j=1}^N \sum_{k=1}^K q_{jk} |\beta_j(\mathbf{x}) - \mathcal{I}_{\Phi_k, \mathbf{X}_n} \beta_j(\mathbf{x})| v_j(\mathbf{s}) \\
&\leq \sum_{j=1}^N \sum_{k=1}^K q_{jk} P_{\Phi_k, \mathbf{X}_n}(\mathbf{x}) \|\beta_j\|_{\mathcal{N}_{\Phi_k(\chi)}} v_j(\mathbf{s}) \\
&\leq C \max_{j \leq N} \left( \sum_{k=1}^K q_{jk} P_{\Phi_k, \mathbf{X}_n}(\mathbf{x}) \right) \max_{j \leq N; k \leq K} (\|\beta_j\|_{\mathcal{N}_{\Phi_k(\chi)}} v_j(\mathbf{s})) \\
&\leq C_\chi \left( \sum_{k=1}^K q_{jk} \right) h_{\mathbf{X}_n}^\nu \max_{j \leq N; k \leq K} (\|\beta_j\|_{\mathcal{N}_{\Phi_k(\chi)}} v_j(\mathbf{s})) \\
&\leq C_\chi h_{\mathbf{X}_n}^\nu \max_{j \leq N; k \leq K} (\|\beta_j\|_{\mathcal{N}_{\Phi_k(\chi)}} v_j(\mathbf{s})),
\end{aligned}$$

where the fourth inequality is because for a fixed  $\mathbf{s}$ , only a constant number (not related to  $N$ ) of  $v_j(\mathbf{s})$  is non-zero, given the mesh is regular. The last inequality holds because  $\sum_{k=1}^K q_{jk} = 1$ . Thus, by taking integral on both sides, and note that

$$\int_{\Omega} \max_{j \leq N} v_j(\mathbf{s}) d\mathbf{s} \leq \max_{j \leq N} \|v_j\|_{L_\infty},$$

it follows that

$$\|u_N - \hat{u}_N\|_{L_2(\Omega, \chi)} \leq C_\chi h_{\mathbf{X}_n}^\nu \max_{j \leq N; k \leq K} (\|\beta_j\|_{\mathcal{N}_{\Phi_k(\chi)}} \|v_j\|_{L_\infty(\Omega)}),$$

which finishes the proof.  $\square$

The theorem indicates that, given the shape functions  $\{v_j\}_{j=1}^N$ , the emulation error is influenced by the two components: the fill distance  $h_{\mathbf{X}_n}$  and  $\max_{j \leq N, k \leq K} (\|\beta_j\|_{\mathcal{N}_{\Phi_k(\chi)}})$ . This is because  $\max_{j \leq N, k \leq K} (\|\beta_j\|_{\mathcal{N}_{\Phi_k(\chi)}} \|v_j\|_{L_\infty(\Omega)}) \leq \max_{j \leq N, k \leq K} (\|\beta_j\|_{\mathcal{N}_{\Phi_k(\chi)}}) \max_{j \leq N} (\|v_j\|_{L_\infty(\Omega)})$ , and  $\max_{j \leq N} (\|v_j\|_{L_\infty(\Omega)})$  often can be upper bounded by a constant once the form of the shape function is given. For instance, if the shape function takes the form as in (3),

$\max_{j \leq N}(\|v_j\|_{L^\infty(\Omega)})$  is upper bounded by 1. For a quasi-uniform design (Wendland, 2004),  $h_{\mathbf{x}_n} \leq Cn^{-1/p}$  for some constant  $C$ , resulting in the emulation error decreasing at the rate  $\nu/p$  with increasing sample size  $n$ . Under certain regularity conditions, the second component,  $\max_{j \leq N, k \leq K}(\|\beta_j\|_{\mathcal{N}_{\Phi_k(\chi)}})$ , can be bounded by a constant for particular PDE systems. An important class of PDEs, *elliptic equations*, is demonstrated in the next section, which provides valuable insights about the error rate with respect to different mesh specifications, PDE problems, and input designs.

## S5 Uncertainty quantification with application to elliptic equations

To demonstrate the error bounds developed in S3 and S4, we apply these error bounds to an important class of PDEs called *elliptic equations*, which is commonly used to describe phenomena that do not change from moment to moment, as when a flow of heat or fluid takes place within a medium with no accumulations (Arnold, 2012; Evans, 2010). Specifically, the elliptic equations have the general form:

$$\operatorname{div} a(\mathbf{s}, \mathbf{x}) \operatorname{grad} u(\mathbf{s}, \mathbf{x}) + c(\mathbf{s}, \mathbf{x})u(\mathbf{s}, \mathbf{x}) = f(\mathbf{s}, \mathbf{x}), \mathbf{s} \in \Omega. \quad (\text{S5.12})$$

Consider (S5.12) with the homogeneous Dirichlet boundary condition:  $u = 0$  on  $\partial\Omega$ . Assume that  $a(\cdot, \mathbf{x}) \in C^1(\bar{\Omega})$ ,  $c(\cdot, \mathbf{x}) \in C(\bar{\Omega})$ ,  $u(\cdot, \mathbf{x}) \in C^2(\bar{\Omega})$  satisfy the PDE and boundary condition, and there exist some constants  $\underline{a}, \bar{a}, \bar{c}$  such that  $0 < \underline{a} \leq a(\cdot, \mathbf{x}) \leq \bar{a}$ ,  $0 \leq c(\cdot, \mathbf{x}) \leq \bar{c}$ , for all  $\mathbf{x} \in \chi$ . Since  $a(\cdot, \mathbf{x})$ ,  $c(\cdot, \mathbf{x})$ ,  $u(\cdot, \mathbf{x})$  satisfy the PDE and boundary condition, they also satisfy the weak formulation,

$$\int_{\Omega} (a(\mathbf{s}, \cdot) \operatorname{grad} u(\mathbf{s}, \cdot) \cdot \operatorname{grad} v(\mathbf{s}) + c(\mathbf{s}, \cdot)u(\mathbf{s}, \cdot)v(\mathbf{s}))d\mathbf{s} = \int_{\Omega} f(\mathbf{s}, \cdot)v(\mathbf{s})d\mathbf{s}, v \in H^1(\Omega). \quad (\text{S5.13})$$

Suppose that the simulation output  $u_N(\mathbf{s}, \mathbf{x})$  in (2) is the solution to the discrete version of (S5.13). Then, the simulation error can be bounded as in (S3.7) with  $r_1 = r_2 := r + 1$  with a positive  $r$  (Arnold, 2012). To show the emulation error bound, we first show that  $\|\beta_j\|_{\mathcal{N}_{\Phi_k(\chi)}}$  in (S4.9) is bounded in the following proposition.

**Proposition S5.1.** *Define the bilinear form*

$$B_{\mathbf{x}}(u(\cdot, \mathbf{x}), v) = \int_{\Omega} (a(\mathbf{s}, \mathbf{x}) \operatorname{grad} u(\mathbf{s}, \mathbf{x}) \cdot \operatorname{grad} v(\mathbf{s}) + c(\mathbf{s}, \mathbf{x}) u(\mathbf{s}, \mathbf{x}) v(\mathbf{s})) d\mathbf{s}.$$

Suppose  $\|D^{\alpha} B_{\mathbf{x}}\|$  and  $\|D^{\alpha} f(\cdot, \mathbf{x})\|_{L_{\infty}(\Omega)}$  are bounded above for any  $\mathbf{x} \in \chi$  and any  $|\alpha| \leq M$  with some integer  $M > \nu + p/2$ , where  $D^{\alpha}$  is weak  $\alpha$ -th partial derivative with respect to  $\mathbf{x}$ . Then for any  $k = 1, \dots, N$ , it follows that  $\|\beta_j\|_{\mathcal{N}_{\Phi_k}(\chi)} \leq C$  with a constant  $C$  that is independent of  $N$ .

*Proof.* We first note that Sobolev space  $H^{\nu+p/2}(\Omega)$  coincides with the reproducing kernel Hilbert space  $\mathcal{N}_{\Phi_k}(\Omega)$  (Wendland (2004), Corollary 10.13). Therefore, since  $\chi$  is compact, it suffices to show that there exists a constant  $C_1$  such that

$$|D^{\alpha} \beta_j(\mathbf{x})| \leq C_1$$

for any  $|\alpha| \leq M$ , any  $\mathbf{x} \in \chi$ , and any  $k \leq N$ .

For a function  $g \in L_2(\Omega)$  such that  $\|D^{\alpha} g\|_{L_{\infty}(\Omega)} < \sup_{\mathbf{x} \in \chi} \|D^{\alpha} f(\cdot, \mathbf{x})\|_{L_{\infty}(\Omega)}$ , define

$$\varepsilon(u(\cdot, \mathbf{x})) = \frac{1}{2} B_{\mathbf{x}}(u(\cdot, \mathbf{x}), u(\cdot, \mathbf{x})) - \langle g(\cdot), u(\cdot, \mathbf{x}) \rangle,$$

where  $\langle \cdot, \cdot \rangle$  is the inner product in  $L_2(\Omega)$ . Define the weak solution  $w_N(\cdot, \mathbf{x})$  as the minimizer of  $\varepsilon(u(\cdot, \mathbf{x}))$  over the space  $V_N(\Omega) := \operatorname{span}(v_1, \dots, v_N)$ , i.e.,

$$w_N(\cdot, \mathbf{x}) = \operatorname{argmin}_{u(\cdot, \mathbf{x}) \in V_N(\Omega)} \varepsilon(u(\cdot, \mathbf{x})). \quad (\text{S5.14})$$

Let  $\mathbf{A}_{\mathbf{x}} \in \mathbb{R}^{N \times N}$  with  $(\mathbf{A}_{\mathbf{x}})_{i,j} = (B_{\mathbf{x}}(v_i, v_j))_{i,j}$ , and  $G = (\langle g, v_1 \rangle, \dots, \langle g, v_N \rangle)^T$ . Then, the minimization problem (S5.14) can be written in a matrix form as  $w_N(\cdot, \mathbf{x}) = \mathbf{w}_N(\mathbf{x})^T \mathbf{v}$ , where

$$\mathbf{w}(\mathbf{x}) = \operatorname{argmin}_{\boldsymbol{\beta} \in \mathbb{R}^N} \frac{1}{2} \boldsymbol{\beta}^T \mathbf{A}_{\mathbf{x}} \boldsymbol{\beta} - G^T \boldsymbol{\beta}, \quad (\text{S5.15})$$

and  $\mathbf{v} = (v_1, \dots, v_N)^T$ . By analysis of finite element methods (see, e.g., Arnold (2012)), it follows that  $\|w_N(\cdot, \mathbf{x})\|_{H^1(\Omega)} \leq C_2$ , for any  $g \in L_2(\Omega)$  such that  $\|D^{\alpha} g\|_{L_{\infty}(\Omega)} < \sup_{\mathbf{x} \in \chi} \|D^{\alpha} f(\cdot, \mathbf{x})\|_{L_{\infty}(\Omega)}$ .

By direct calculation and the minimizer of (S5.15), we have

$$\varepsilon_{\mathbf{x}}^* := \min_{u(\cdot, \mathbf{x}) \in V_N(\Omega)} \varepsilon(u(\cdot, \mathbf{x})) = -\frac{1}{2} G^T \mathbf{A}_{\mathbf{x}}^{-1} G. \quad (\text{S5.16})$$

Then, by analysis of finite element methods, it follows that  $\varepsilon_{\mathbf{x}}^* \leq C_3$  for any  $g \in L_2(\Omega)$  such that  $\|D^\alpha g\|_{L_\infty(\Omega)} < \sup_{\mathbf{x} \in \chi} \|D^\alpha f(\cdot, \mathbf{x})\|_{L_\infty(\Omega)}$ .

Taking the derivative of  $\varepsilon_{\mathbf{x}}^*$  with respect to  $\mathbf{x}$  yields

$$|D^\alpha \varepsilon_{\mathbf{x}}^*| = \frac{1}{2} G^T D^\alpha \mathbf{A}_{\mathbf{x}}^{-1} G = D^\alpha B_{\mathbf{x}}(w_N(\cdot, \mathbf{x}), w_N(\cdot, \mathbf{x})) \leq C_4, \quad (\text{S5.17})$$

where the last inequality holds because  $\|D^\alpha B_{\mathbf{x}}\|$  is bounded. Since (S5.17) is true for any  $g \in L_2(\Omega)$  such that  $\|D^\alpha g\|_{L_\infty(\Omega)} < \sup_{\mathbf{x} \in \chi} \|D^\alpha f(\cdot, \mathbf{x})\|_{L_\infty(\Omega)}$ , we have  $\|D^\alpha \mathbf{A}_{\mathbf{x}}^{-1}\|_2 \leq C_5$  for any  $|\alpha| \leq M$ .

Recall  $\beta_N(\mathbf{x}) = (\beta_1(\mathbf{x}), \dots, \beta_N(\mathbf{x}))^T$ . By analysis of finite element methods, we have  $\beta_N(\mathbf{x}) = \mathbf{A}_{\mathbf{x}}^{-1} F_{\mathbf{x}}$ , where  $F_{\mathbf{x}} = (\langle f(\cdot, \mathbf{x}), v_1 \rangle, \dots, \langle f(\cdot, \mathbf{x}), v_N \rangle)^T$ . Thus, by Newton-Leibniz formula, it follows that

$$\begin{aligned} |D^\alpha \beta_j(\mathbf{x})| &= |\mathbf{e}_j^T D^\alpha (\mathbf{A}_{\mathbf{x}}^{-1} F_{\mathbf{x}})| \\ &\leq C_5 \sum_{\alpha_1 \leq \alpha} \|D^{\alpha_1} \mathbf{A}_{\mathbf{x}}^{-1}\|_2 \|D^{\alpha - \alpha_1} F_{\mathbf{x}} \mathbf{e}_j^T\|_2 \\ &\leq C_6, \end{aligned}$$

where  $\mathbf{e}_j$  is a unit vector with the  $j$ -th element being one. The last inequality holds because  $\sup_{\theta \in \Theta} \|D^\alpha f(\cdot, \mathbf{x})\|_{L_\infty(\Omega)}$  is bounded. This finishes the proof.  $\square$

Moreover, for FEM simulations, it follows that  $\|v_j\|_{L_2(\Omega)} < C$  for a constant  $C$ . We now combine this result and Proposition S5.1 with Theorem S4.1. Together with the simulation error bound (S3.7), it gives the following corollary.

**Corollary S5.2.** *Suppose the conditions of Theorem S4.1 and Proposition S5.1 hold. Assume that  $\|u_0(\cdot, \mathbf{x})\|_{H^{r+1}(\Omega)} \leq C$  with a constant  $C$  and the true solution  $u_0(\cdot, \mathbf{x}) \in H^{r+1}(\Omega)$  for all  $\mathbf{x} \in \chi$ , then the emulator  $\hat{u}_N(\mathbf{s}, \mathbf{x})$  for the solutions to elliptic equations has the error*

bound:

$$\|u_0 - \hat{u}_N\|_{L_2(\Omega, \chi)} \leq C_\chi h_{\mathbf{X}_n}^\nu + C_\Omega h_{\mathcal{T}_N}^{r+1}. \quad (\text{S5.18})$$

Corollary S5.2 implies that, for elliptic equations, with a fixed mesh specification, the error of the emulator  $\hat{u}_N(\mathbf{s}, \mathbf{x})$  decreases at the rate  $\nu$  with increasing fill distances of  $\mathbf{X}_n$  in the space  $\chi$ , and with a fixed input design  $\mathbf{X}_n$ , the error decreases at the rate  $r + 1$  with increasing mesh sizes.

**Example S5.3** A simulation study is conducted here to verify the rate of convergence given in Corollary S5.2. We consider the Poisson's equation in Section 5.1, which is an elliptic equation. The equation has an analytical solution, as derived in Tuo et al. (2014), which is

$$u_0(\mathbf{s}, x) = e^{xs_1} \sin(\pi s_1) \sin(\pi s_2),$$

making it possible to analyze the error bound of (S5.18).

We consider a set of sample sizes,  $n = 5, 10, 15, 20$ , and  $25$ , which yields the fill distances  $h_{\mathbf{X}_n} = \frac{1}{2}, \frac{1}{4.5}, \frac{1}{7}, \frac{1}{9.5}$  and  $\frac{1}{12}$ , respectively. Moreover, for each sample size, we consider a set of mesh sizes,  $h_{\mathcal{T}_N} = 0.4, 0.2, 0.1, 0.5$ , and  $0.025$ . We conduct a finite element simulation for each  $h_{\mathbf{X}_n}$  and  $h_{\mathcal{T}_N}$ . Based on the simulations, we perform the **mcGP** method using the Matérn correlation function (7) with  $\nu = 2.5$  to obtain  $\hat{u}_N$  and then compute  $E = \|u_0 - \hat{u}_N\|_{L_2(\Omega, \chi)}$ , where the  $L_2$ -norm is approximated by Monte Carlo integration. We then consider the regression problem,

$$E_{ij} = a(h_{\mathbf{X}_n})_i^\nu + b(h_{\mathcal{T}_N})_j^{r+1} + e_{ij},$$

for  $i = 1, \dots, 5$  and  $j = 1, \dots, 5$ . The coefficients  $a$  and  $b$  can be estimated by the least squares method for a fixed  $\nu$  and  $r$ . For the estimates of  $\nu$  and  $r$ , we constrain them as integers and use a grid search to identify the values that yield the highest R-squared value. Figure S16 demonstrates the errors  $E_{ij}$ , along with the fitted regression lines. The estimation results are as follows:  $\hat{a} = 0.0044, \hat{b} = 0.1453, \hat{\nu} = 3$  and  $\hat{r} = 2$ . It appears that the fitted regression lines are closely aligned with the  $L_2$  errors, providing validation for the convergence rate stated in Corollary S5.2, as the theoretical assertion is  $\nu = 2.5$  and  $r = 2$  given the adoption of the quadratic shape functions (Brenner and Scott, 2007).



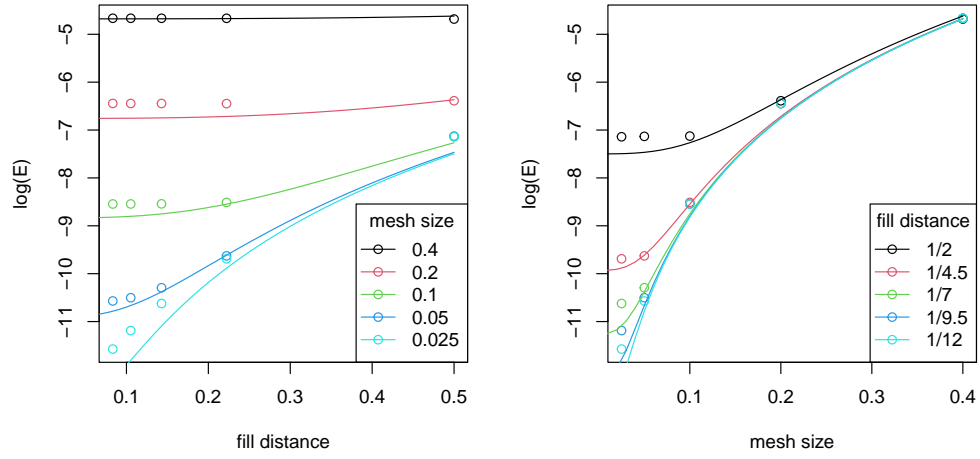


**Figure S16:** The  $L_2$  errors (dots) with respect to the fill distance  $h_{\mathbf{X}_n}$  and the mesh size  $h_{\mathcal{T}_N}$ , along with the fitted regression lines.